School of Science
Department of Physics and Astronomy
Master Degree in Physics

# Low density ferrromagnetism in a square-to-triangular lattice

Supervisor Prof. Pierbiagio Pieri Submitted by: JingHao Wang

# Abstract

This thesis investigates the emergence of ferromagnetism in two-dimensional Hubbard models on geometrically frustrated lattices, focusing on the continuous transition from square to triangular geometries. The motivation comes from recent progress in ultracold atom experiments, where lattice geometry can be tuned with high precision, opening new possibilities to study frustration-driven quantum magnetism. We employ the T-matrix approximation to analyze the competition between kinetic energy, interaction strength, and lattice frustration at low particle densities. By extending the T-matrix framework to both finite lattices and the thermodynamic limit, we perform accurate energy comparisons between paramagnetic and ferromagnetic states. Our results yield phase diagrams that map out the conditions for the stabilization of ferromagnetism as frustration is varied, providing theoretical guidance for experiments with ultracold optical lattices and offering new insights into the microscopic mechanisms of itinerant ferromagnetism.

# Introduction

Magnetism in strongly correlated systems has been a central theme of condensed matter physics for decades. Ferromagnetism, characterized by the spontaneous alignment of electron spins, is one of the most fundamental yet least understood phenomena in itinerant systems. The Hubbard model, which captures the competition between kinetic energy and on-site repulsion, offers a minimal framework for addressing this issue. However, despite decades of study, consensus on the microscopic origin and stability of ferromagnetism in the Hubbard model remains elusive [1, 2, 3].

Frustrated lattice geometries play a decisive role in this problem. While bipartite lattices such as the square lattice favor antiferromagnetic correlations near half filling, triangular lattices suppress them and may enhance ferromagnetic tendencies. Recent progress in ultracold atom experiments has made it possible to continuously tune the lattice from square to triangular geometry[4], providing an ideal setting for exploring frustration-driven magnetism at low densities.

Theoretical studies of ferromagnetism in the Hubbard model have employed diverse approaches, including quantum Monte Carlo simulations [5, 6, 7, 8], dynamical mean-field theory [9, 10, 11], and diagrammatic Monte Carlo [12, 13]. These methods provide valuable insights but face challenges such as finite-size effects, the fermionic sign problem, or overestimation of ferromagnetic regions. Experimentally, ultracold atomic gases in optical lattices [14] offer unprecedented control of density, interactions, and geometry, yet clear evidence of itinerant ferromagnetism remains lacking due to competing phases and finite-temperature effects.

The goal of this thesis is to investigate ferromagnetism in the two-dimensional Hubbard model at low densities, focusing on the square-to-triangular lattice transition. We employ the T-matrix approximation to compute the ground-state energy of paramagnetic and ferromagnetic states. Numerical algorithms are developed and optimized for parallel computation, enabling detailed analysis of the interplay between density, interaction strength, and frustration.

The remainder of the thesis is organized as follows. Chapter 1 introduces the Hubbard model, the physics of itinerant ferromagnetism, and the motivation for studying tunable frustrated lattices. Chapter 2 presents the T-matrix formalism

and its application to both finite and infinite systems. Chapter 3 describes the numerical implementation. Chapter 4 discusses the results and phase diagrams. Chapter 5 summarizes the conclusions and provides an outlook for future work.In the appendix, we provide a detailed description of several numerical methods employed in this study.

# Contents

Introduction					
1	Ferromagnetism in the lattice model				
	1.1	General properties of the Hubbard Model	1		
	1.2	Ferromagnetism in the Hubbard Model	4		
	1.3	From Square to triangular lattice	10		
	1.4	Further recent experimental works	15		
<b>2</b>	The	oretical approach to ferromagnetism in frustrated lattice	17		
	2.1	T-matrix approximation	17		
		2.1.1 Two-electron Hamiltonian and Hartree–Fock approximation	18		
		2.1.2 T-matrix approximation for the paramagnetic energy	20		
	2.2	T-matrix Approach to Ferromagnetism in Iron-Series Metals	24		
	2.3	TMA calculation for Lattices	29		
		2.3.1 Finite case	29		
		2.3.2 Thermodynamic limit case	30		
	2.4	Lattice models and dispersion relations	32		
		2.4.1 Two Diagonal Hopping case	32		
		2.4.2 One Diagonal Hopping case	34		
3	Nui	nerical Methods	38		
	3.1	Structure and parameter	38		
		3.1.1 Computational Framework and Parameter Settings	38		
	3.2	Energy Spectrum and Fermi Distribution	39		
		3.2.1 Dispersion Relations	39		
		3.2.2 Energy Sorting and Lookup Tables	40		
		3.2.3 Zero-Temperature Fermi Distribution	41		
	3.3	Energy Calculation Methods	42		
		3.3.1 Free Energy Term	42		
		3.3.2 Interaction Energy Term	43		
		3.3.3 Numerical Optimizations	44		
		*			

CONTENTS

#### CONTENTS

	3.4	Determination of lowest energy phase and Parallel Computing					
		3.4.1	Energy Comparison Between Ferromagnetic and Paramag-				
			netic States	46			
		3.4.2	Phase Determination Strategies				
		3.4.3	Parallelization Implementation				
4	Numerical Results and Analysis 4						
	4.1	Finite	Lattice Calculations	49			
		4.1.1	Two-Diagonal Hopping Case	49			
		4.1.2	One-Diagonal Hopping Case	53			
	4.2	Thern	nodynamic Limit Analysis				
		4.2.1	Two-Diagonal Hopping Case				
		4.2.2	One-Diagonal Hopping case				
5	Conclusions and Outlooks						
	5.1	Concl	usions	68			
	5.2		oks				
$\mathbf{A}_{\mathbf{J}}$	ppen	dix I					
	Monte Carlo Integration						
$\mathbf{A}_{\mathbf{J}}$	ppen	dix II					
	$\operatorname{Bre}$	nt's M	lethod for Root-Finding	<b>75</b>			
Bi	Bibliography						
A	Acknowledgements						

CONTENTS

# Chapter 1

# Ferromagnetism in the lattice model

This chapter introduces the theoretical and experimental background of ferromagnetism in lattice models. We begin with the Hubbard model as the minimal framework for describing correlated electrons, followed by an explanation of the microscopic mechanism that stabilizes ferromagnetic order. We then discuss recent experimental advances in tuning lattice geometry from square to triangular configurations, which provide a versatile platform for investigating frustration effects. Finally, we review recent progress in the field, with a focus on emergent ferromagnetic phases in frustrated lattices and their implications for future studies.

### 1.1 General properties of the Hubbard Model

Ferromagnetism is one of the most important and complex collective phenomena in strongly correlated systems, and its origin has long attracted extensive attention in condensed matter physics and many-body theoretical research[2, 15, 3]. The Hubbard model, as the theoretical framework for describing strongly correlated systems, has played a central role in exploring the microscopic mechanisms of itinerant ferromagnetism. The Hubbard model was first proposed by Hubbard, Kanamori, and Gutzwiller in 1963[16, 17, 18], to describe interacting electrons in transition metals and their oxides, and to understand the magnetic properties and

metal-insulator transitions in such systems.

The general form of the Hubbard Hamiltonian on a lattice can be written as

$$H = -\sum_{i,j,\sigma} t_{ij} c_{i,\sigma}^{\dagger} c_{j,\sigma} + U \sum_{i} \hat{n}_{i\uparrow} \hat{n}_{i\downarrow}, \qquad (1.1)$$

where i and j are lattice indices, and  $\sigma$  denotes the spin index. The hopping term includes contributions from nearest-neighbor (generally denoted as t) and next-nearest-neighbor (generally denoted as t') interactions as shown in Figure 1.1, while U represents the on-site Coulomb interaction.

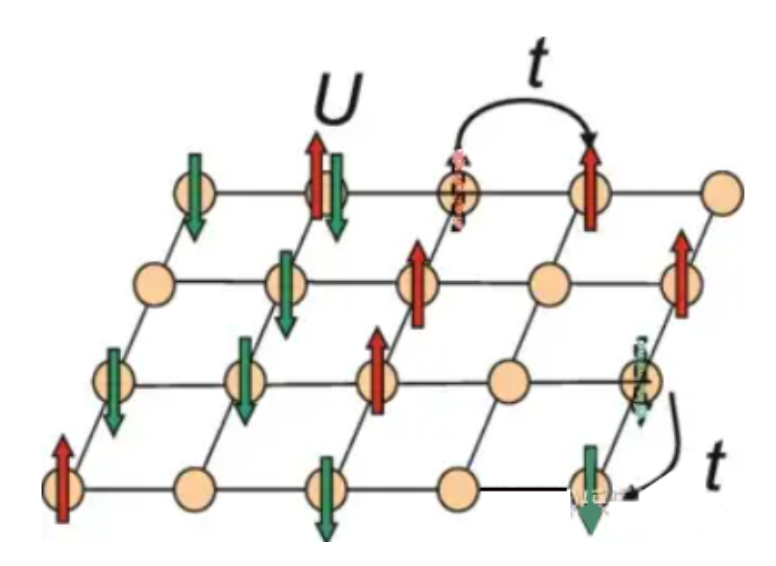


Figure 1.1. The nearest hopping parameter t in Hubbard model.

The kinetic energy term (hopping term), characterized by the hopping amplitude  $t_{ij}$ . It allows fermions to move between lattice sites i and j, and encodes the geometry and dimensionality of the underlying lattice. In most cases, one considers nearest-neighbor hopping t, and sometimes next-nearest-neighbor hopping t' in order to account for frustration and more realistic band structures. The on-site interaction term  $U \sum_i \hat{n}_{i\uparrow} \hat{n}_{i\downarrow}$ , which penalizes double occupation of the same lattice site. This term captures the essence of electronic correlations arising from the Coulomb repulsion in real materials.

The competition between kinetic energy (favoring delocalization) and interaction energy (favoring localization) lies at the heart of the Hubbard model. In the

weak-coupling limit  $U/t \ll 1$ , the system behaves similarly to a Fermi liquid, where electrons are itinerant and weakly correlated. In contrast, in the strong-coupling limit  $U/t \gg 1$ , double occupation is strongly suppressed, and at half-filling the system becomes a Mott insulator. In this limit, an effective low-energy description is given by the antiferromagnetic Heisenberg spin Hamiltonian

$$\hat{H}_{\text{eff}} = J \sum_{\langle i,j \rangle} \hat{\mathbf{S}}_i \cdot \hat{\mathbf{S}}_j, \quad J = \frac{4t^2}{U},$$
 (1.2)

where  $\hat{\mathbf{S}}_i$  is the spin operator at site *i*. This mapping reveals the deep connection between the Hubbard model and quantum magnetism.

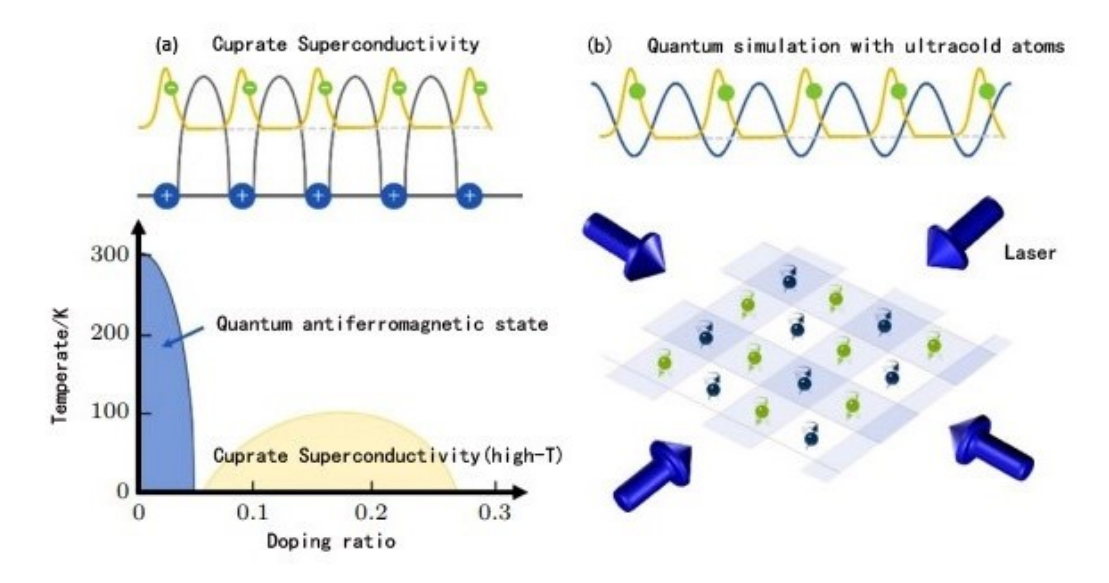


**Figure 1.2.** Illustration of the ultracold atom simulation for the Fermi-Hubbard model, ultracold atoms serve as analogues of electrons in condensed matter systems, with optical standing waves forming lattice structures.

From a modern perspective, the Hubbard model is not only a paradigm for strongly correlated electrons in solids, but also serves as the central theoretical framework for quantum simulations with ultracold atoms in optical lattices. In 1995, Bose-Einstein condensation of alkali-metal atoms was experimentally achieved [19], marking the beginning of a new era in the field of ultracold atomic physics. Soon after, the realization of the Hubbard model with ultracold atoms was pro-

posed [20].

As shown in Figure 1.2, this theoretical scheme ingeniously maps atoms to the role of electrons in condensed matter systems and employs standing-wave laser fields to construct an "optical lattice," thereby laying the foundation for quantum simulation of strongly correlated models. In 1999, a degenerate Fermi gas was experimentally realized for the first time [21], which made the quantum simulation of the Fermi-Hubbard model feasible. In such setups, the hopping amplitude t, interaction strength U, and even the lattice geometry can be tuned almost arbitrarily, providing unprecedented control to test theoretical predictions and probe regimes that are challenging for numerical or analytical methods.

The Hubbard model provides a minimal yet powerful description of interacting fermions on a lattice. Its Hamiltonian encodes the competition between itinerancy and interactions, and gives rise to a variety of emergent phases, including Mott insulators, magnetically ordered states, and possible ferromagnetic phases at low densities. This makes it the natural starting point for investigating the problem of low-density ferromagnetism in two-dimensional lattices.

#### 1.2 Ferromagnetism in the Hubbard Model

To better understand the ferromagnetism, mean-field approximation is a good approach. The key idea is that the Hubbard repulsion U may favor a ferromagnetic order, as this configuration minimizes the Coulomb repulsion between electrons. To implement the mean-field approximation, we decompose each spin density operator into its average value and a fluctuating component. Specifically, we set

$$\hat{n}_{i\uparrow} = \bar{n}_{i\uparrow} + (\hat{n}_{i\uparrow} - \bar{n}_{i\uparrow}) = \bar{n}_{i\uparrow} + \delta \hat{n}_{i\uparrow}$$
(1.3)

where  $\bar{n}_{i\uparrow}$  represents the average (mean-field) value of the spin-up density, and  $\delta \hat{n}_{i\uparrow}$  accounts for deviations from this average. We perform the same decomposition for the spin-down density  $\hat{n}_{i\downarrow}$ . With these decompositions, we can approximate the interaction term in the Hamiltonian by neglecting higher-order fluctuation terms. In particular, we discard the product of fluctuations  $\delta \hat{n}_{i\uparrow} \delta \hat{n}_{i\downarrow}$  (referred to as the "square of deviation from average") under the mean-field assumption that fluctu-

ations are small compared to the average values. This leads to the approximation:

$$\hat{n}_{i\uparrow}\hat{n}_{i\downarrow} \simeq \bar{n}_{i\uparrow}\bar{n}_{i\downarrow} + (\hat{n}_{i\uparrow} - \bar{n}_{i\uparrow})\bar{n}_{i\downarrow} + (\hat{n}_{i\downarrow} - \bar{n}_{i\downarrow})\bar{n}_{i\uparrow}$$

$$= \hat{n}_{i\uparrow}\bar{n}_{i\downarrow} + \hat{n}_{i\downarrow}\bar{n}_{i\uparrow} - \bar{n}_{i\uparrow}\bar{n}_{i\downarrow}$$
(1.4)

Next, we parameterize the average spin densities to explicitly account for possible ferromagnetic order. We define:

$$\bar{n}_{i\uparrow} = \frac{n}{2} + m_z \tag{1.5}$$

$$\bar{n}_{i\downarrow} = \frac{n}{2} - m_z \tag{1.6}$$

where n represents the total particle density  $(n = \bar{n}_{i\uparrow} + \bar{n}_{i\downarrow})$  and  $m_z$  denotes the magnetization (net spin density). Importantly, a non-zero value of  $m_z$  indicates that the system is in a ferromagnetic state, as it signifies a imbalance between spin-up and spin-down populations. Substituting these parameterizations into the Hamiltonian and rearranging terms, we obtain:

$$H = \sum_{i,j} t_{ij} c_{i\sigma}^{\dagger} c_{j\sigma} + U \sum_{i} \left[ \hat{n}_{i\uparrow} \left( \frac{n}{2} - m_z \right) + \hat{n}_{i\downarrow} \left( \frac{n}{2} + m_z \right) \right] - UN \left( \frac{n}{2} + m_z \right) \left( \frac{n}{2} - m_z \right)$$

$$(1.7)$$

Here, the last term is a constant (independent of operators) that we denote as  $-C(n, m_z)$ We define:

$$C(n, m_z) = -UN\left[\left(\frac{n}{2}\right)^2 - m_z^2\right]$$
(1.8)

To simplify further, we transform the Hamiltonian into momentum  $(\hat{k})$  space, where the kinetic energy term diagonalizes. This leads to:

$$\hat{H} = \sum_{\vec{k},\sigma} \varepsilon_{\vec{k}} c_{\vec{k}\sigma}^{\dagger} c_{\vec{k}\sigma} + U\left(\frac{n}{2} - m_z\right) \sum_{\vec{k}} c_{\vec{k}\uparrow}^{\dagger} c_{\vec{k}\uparrow} + U\left(\frac{n}{2} + m_z\right) \sum_{\vec{k}} c_{\vec{k}\downarrow}^{\dagger} c_{\vec{k}\downarrow} - C(n, m_z)$$

$$(1.9)$$

We can now combine the kinetic and interaction terms by defining a renormal-

ized dispersion relation for each spin species:

We define

$$\varepsilon_{\vec{k}\sigma} = \varepsilon_{\vec{k}} + \frac{Un}{2} - \xi_{\sigma}Um_z \quad \text{with } \xi_{\uparrow} = +1, \xi_{\downarrow} = -1$$
 (1.10)

This allows us to rewrite the Hamiltonian in the compact form:

$$H = \sum_{\vec{k},\sigma} \varepsilon_{\vec{k}\sigma}^{\dagger} c_{\vec{k}\sigma}^{\dagger} c_{\vec{k}\sigma} - C(n, m_z)$$
(1.11)

At zero temperature (T=0), the occupation of each momentum state is determined by the Fermi-Dirac distribution, which reduces to a step function  $\Theta(x)$  (1 for x > 0, 0 otherwise). The average spin densities are then given by:

$$m_{\sigma} = \frac{N_{\sigma}}{N} = \frac{1}{N} \sum_{\vec{k}} \Theta(\mu - \varepsilon_{\vec{k}\sigma}) = \int d\varepsilon \tilde{\mathcal{N}}(\varepsilon) \Theta\left(\mu - \varepsilon - \frac{Un}{2} + \xi_{\sigma} U m_z\right)$$
(1.12)

where  $\Theta(x)$  is the step function,  $\mu$  is the chemical potential, and  $\tilde{\mathcal{N}}(\varepsilon) = a^3 \mathcal{N}(\varepsilon)$  denotes the density of states per spin per site. The magnetization  $m_z$  is the difference between the spin-up and spin-down densities, divided by 2:

$$\frac{m_{\uparrow} - m_{\downarrow}}{2} = m_z = \frac{1}{2} \int d\varepsilon \tilde{\mathcal{N}}(\varepsilon) \left[ \Theta\left(\mu - \varepsilon - \frac{Un}{2} + Um_z\right) - \Theta\left(\mu - \varepsilon - \frac{Un}{2} - Um_z\right) \right]$$
(1.13)

To determine when a ferromagnetic solution  $(m_z \neq 0)$  is possible, we consider the case of small  $m_z$  and linearize the step functions around their arguments. This linearization uses the property that the derivative of the step function is a delta function,  $\Theta'(x) = \delta(x)$ , leading to:

$$m_z = \frac{1}{2} \int d\varepsilon \tilde{\mathcal{N}}(\varepsilon) \Theta' \left( \mu - \varepsilon - \frac{Un}{2} \right) \cdot 2Um_z$$
 (1.14)

Substituting  $\Theta'(x) = \delta(x)$  and evaluating the integral, we find:

$$m_z = \tilde{\mathcal{N}} \left( \mu - \frac{Un}{2} \right) U m_z \tag{1.15}$$

where  $\varepsilon_F$  (the Fermi energy of the non-interacting system) is identified with  $\mu - \frac{Un}{2}$  in this context. For a non-trivial solution  $(m_z \neq 0)$  to exist, we must have:

$$1 = \tilde{\mathcal{N}}(\varepsilon_F)U \tag{1.16}$$

This condition defines the critical value of U above which ferromagnetic order emerges. Known as the "Stoner criterion," [22] it highlights that ferromagnetism arises when the product of the Hubbard repulsion and the density of states at the Fermi level exceeds unity.

Ferromagnetism in the Hubbard model primarily arises from the delicate balance between interaction energy and kinetic energy induced by spin polarization. At low densities, the average spatial separation between electrons is relatively large, and thus the energetic cost associated with double occupancy becomes comparatively small. In this regime, the ground-state energy of the system consists of two competing contributions: on the one hand, the kinetic energy tends to minimize the Fermi surface volume, favoring an unpolarized state; on the other hand, spin polarization can strongly suppress the probability of double occupancy, thereby reducing the interaction energy. When the energy gain from the latter mechanism outweighs the kinetic cost of polarization, the system undergoes a transition to a spontaneously ferromagnetic state.

Rigorous results can only be obtained for exceptional cases such as Nagaoka ferromagnetism [23, 24, 25]. and flat-band ferromagnetism [26]. Nagaoka ferromagnetism considers a single-hole doping away from half filling in the limit of infinite repulsion, and flatband ferromagnetism requires fine tuning of particle hopping to reach a flat-band dispersion. Moreover, the single-band Hubbard model is usually oversimplified to directly compare with experiments on real materials.

The study of ferromagnetism in the low-density regime of the Hubbard model is of particular significance. In this limit, the competition between electron-electron correlations and kinetic energy becomes extremely delicate, rendering the stabilization of ferromagnetic order highly sensitive and confined to narrow regions of parameter space. An alternative route to ferromagnetism was proposed by Müller-Hartmann [27], who investigated the one-dimensional (1D) Hubbard model with both nearest- and next-nearest-neighbor hopping (the  $t_1$ - $t_2$  Hubbard model). For

infinite U and a band dispersion characterized by two degenerate minima, he found that saturated ferromagnetism can be stabilized at low electron densities. The underlying mechanism is that the Pauli exclusion principle strongly suppresses the probability of double occupancy in a fully spin-polarized state, thereby minimizing the cost of the on-site repulsion U. In this regime, the kinetic energy penalty of polarization remains comparatively small, such that the ferromagnetic configuration can become energetically favorable over the paramagnetic one.

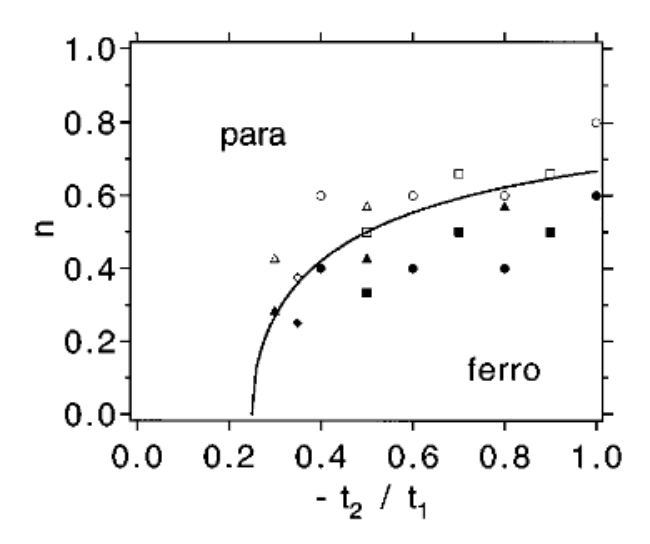


**Figure 1.3.** Phase diagram of the  $t_1$ - $t_2$  Hubbard chain in the  $t_2$ -n plane for  $U \to \infty$ , as obtained by exact diagonalization for finite lengths L. Circles: L=10, squares: L=12, triangles: L=14, diamonds: L=16. Open symbols: paramagnetic ground state, full symbols: ferromagnetic ground state. The full line shows the density where the fully polarized Fermi sea splits into two pockets.

Subsequent numerical studies have further analyzed this ferromagnetism [28]. Exact diagonalization of finite-size 1D chains ( $L \leq 18$ ) with periodic boundary conditions shows that at the lowest accessible density, n = 2/L (two electrons in the chain), the ground state is strictly a triplet, consistent with saturated ferromagnetism. When the Coulomb interaction strength U is sufficiently large, this ferromagnetic state is not confined to the very dilute limit but persists up to a finite critical density  $n_c$ . They found that the critical density  $n_c$  is directly related to the topological structure of the Fermi surface of the fully polarized state. They get the variation curve of  $n_c$  with  $t_2/t_1$  (Figure 1.3) is in good agreement with

the numerical data, confirming the role of Fermi surface topology in 1D ferromagnetism.

To characterize this behavior, a single-spin-flip variational approach was employed to construct trial states  $|\psi_c\rangle$  and evaluate the change of their total energies  $\Delta E$ . Based on this expansion  $\Delta E = -2n\epsilon_0 - \Delta + O(n^{1+2/d})$ , it was shown that in dimensions  $d \geq 3$ , the destabilizing term  $\Delta$  dominates at low densities, rendering ferromagnetism unstable. In one dimension the stabilizing term  $2n\epsilon_0$  prevails while  $\Delta$  contributes only at order  $O(n^2)$ , which is negligible in the dilute limit.

For d=2,  $\Delta$  and the stabilizing contribution  $2n\epsilon_0$  are of the same order. So in this case, in order to examine the viability of the low-density route, they inserting this expression into  $\Delta E = -2n\epsilon_0 - \Delta + O(n^{1+2/d})$  where the  $\Delta = n/\rho(\epsilon_0)$  and  $\rho(\epsilon_0)$  is the density of states at the bottom of the band. Using the stability criterion  $\Delta E > 0$ , they obtain the following necessary condition for the stability of the fully polarized state,

$$2\rho(\epsilon_0)|\epsilon_0| > 1. \tag{1.17}$$

To be specific, they consider the  $t_1$ - $t_2$  Hubbard model on a square lattice. When  $t_2 < -t_1/2$  the band has degenerate minima at the Brillouin zone boundary. It follows from Eq.1.17 that the polarized state cannot be the ground state outside the region  $-0.20t_1 > t_2 > -0.65t_1$ . Hence for  $t_2 < -0.65t_1$  the polarized state is unstable even though there are two minima.

As a result, they conclude that ferromagnetism is naturally favored in 1D, whereas the same mechanism is not allowed in generic three-dimensional systems and is severely restricted in two dimensions.

Recent advances in ultracold atom experiments have also provided a controllable platform to probe strongly correlated systems at low densities[14, 29]. By tuning the filling and interaction strength of fermionic atoms loaded into optical lattices, one can directly simulate low-density ferromagnetism in the Hubbard model under nearly ideal and disorder-free conditions. This not only offers a unique opportunity to benchmark theoretical predictions, but also provides valuable insight into dilute-carrier ferromagnetism in solid-state systems, such as diluted magnetic semiconductors and low-density transition-metal compounds.

In summary, the Hubbard model reveals two essential ingredients for the stabi-

lization of low-density ferromagnetism: the reduction of interaction energy through suppressed double occupancy, and the peculiarities of the band structure that enhance the density of states. In square lattices, triangular lattices, and their interpolating geometries, features such as flat bands, van Hove singularities, and geometric frustration jointly determine the stability region of ferromagnetic order. Research along this line not only deepens our understanding of the microscopic origin of ferromagnetism in strongly correlated systems, but also establishes a theoretical foundation for exploring novel magnetic phases via quantum simulation with ultracold atoms.

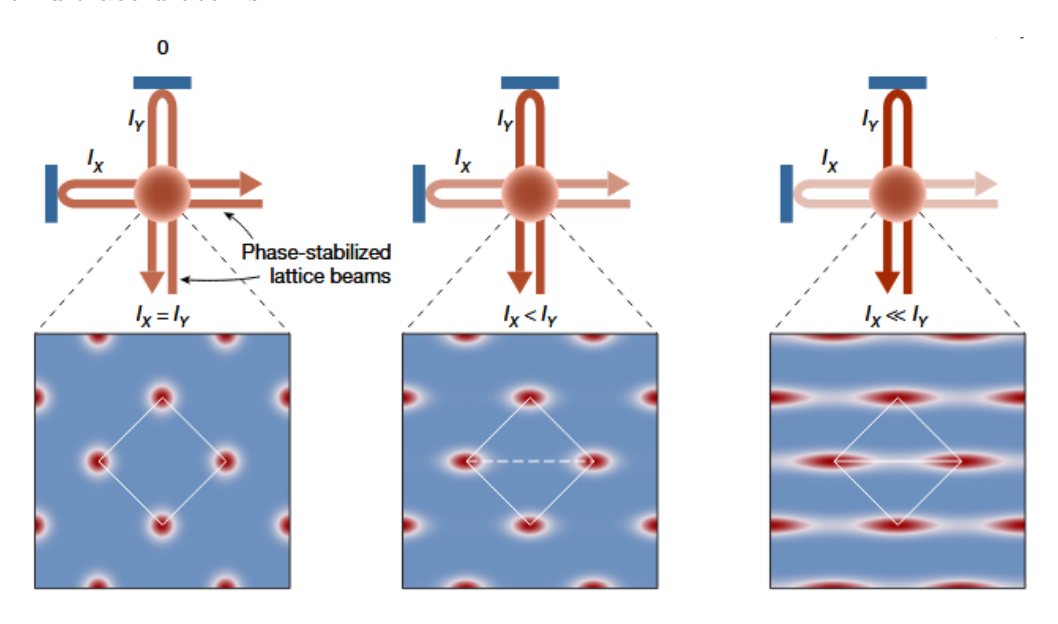


**Figure 1.4.** The lattice formed by the interference of two orthogonal retro-reflected laser beams whose relative phase is actively stabilized.

## 1.3 From Square to triangular lattice

A novel experimental technique enables the continuous tuning of lattice geometry from a square to a frustrated triangular configuration[4]. The system is realized by the interference of two orthogonal retro-reflected laser beams, whose relative phase is actively stabilized[30, 31]. With equal beam intensities, this interference produces a non-separable square lattice rotated by 45°.

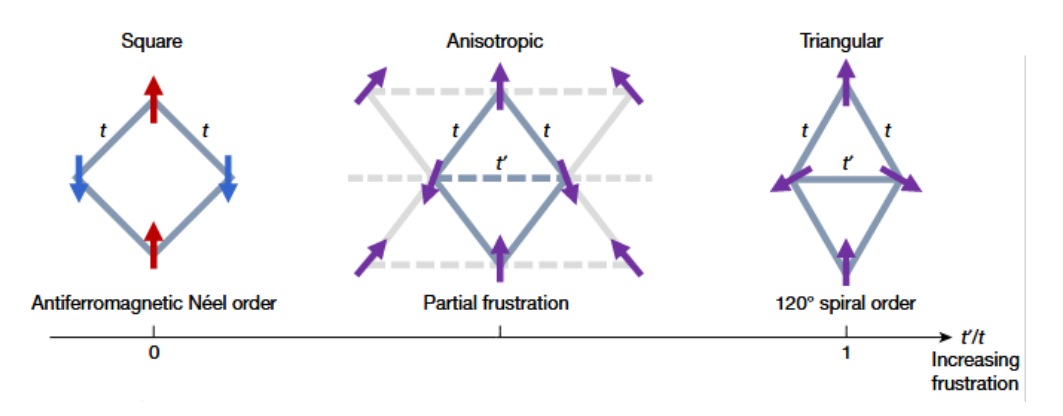


**Figure 1.5.** A square lattice with coupling t can be continuously transformed into a triangular lattice with an extra tunable coupling t' along one diagona.

Frustration is introduced through an additional tunnelling term t' along one diagonal of the square lattice. By adjusting the intensity balance between the two lattice beams, the potential barrier between diagonal neighbours is reduced, thereby enhancing the diagonal tunnelling as shown in Figure 1.4. This implementation differs from previous schemes based on three laser beams with 120° rotational symmetry [32, 33, 34, 35, 36].

The degree of frustration is parameterized by the anisotropy ratio t'/t. As this ratio is tuned, the lattice smoothly evolves from a square geometry at t'/t = 0 to an triangular lattice at t'/t = 1. In both the classical and quantum Heisenberg limits, this tuning drives a change in the magnetic ground state from collinear Néel order on the square lattice to a 120° spiral order on the triangular lattice as shown in Figure 1.5. In the extreme limit  $t'/t \gg 1$ , the system undergoes a dimensional crossover towards weakly coupled one-dimensional chains. This experiment finds ferromagnetic correlation when t'/t > 0.5 and when total fermion density n exceeds half filling n = 1 and is somewhat close to n = 1.5. The regime where ferromagnetism is observed is marked by the shaded yellow area in Figure 1.6. This experiment has only explored the density regime 0.5 < n < 1.5 and it is not clear whether the ferromagnetic correlation can also exist when n exceeds 1.5. The physical origin of this observed ferromagnetism is also not clear yet.

The other article provides a further numerical analysis of this experiment [37]. For the benefit of later discussion, they make a particle-hole transformation  $\hat{c}_{i\sigma} \rightarrow (-1)^{i_x+i_y}\hat{c}_{i\sigma}^{\dagger}$ , where  $i=(i_x,i_y)$  is the site label. Like we discusses before the t' term

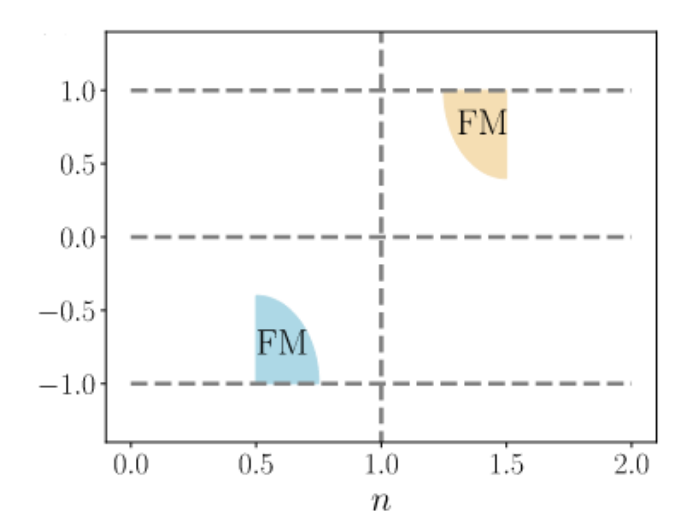


**Figure 1.6.** The ferromagnetic correlation found in the experiment is marked by the shaded yellow regime in the n-t' phase diagram, which is mapped to the shaded blue area under the particle-hole transformation.

is what causes frustration in this lattice, and thus, the t' term is not invariant under the particle-hole transformation. Under this transformation,  $n = n_{\uparrow} + n_{\downarrow}$  becomes 2 - n, that is, the particle doping is mapped to hole doping. Thus, the particle-hole transformation maps (t', n) to (-t', 2-n) in the phase diagram shown in Figure 1.6(b). Therefore, they can focus solely on the density regime  $0 < n \le 1$  but include both positive and negative t'. With this mapping, the regime where ferromagnetism is observed is mapped to the low-density regime with t' < -0.5, as marked as the shaded blue area in Figure 1.6. In their calculation they set interaction strength U is infinite. They use density-matrix renormalization group (DMRG) calculation with a finite number of fermions on a different strip geometry. They can calculate  $\langle \hat{S}_{\text{tot}}^2 \rangle$  with  $\hat{S}_{\text{tot}} = \sum_i \hat{S}_i$  for the ground state, and  $S_{\text{tot}}$  is given by  $\langle \hat{S}_{\text{tot}}^2 \rangle = S_{\text{tot}}(S_{\text{tot}} + 1)$ .

In the calculations they fix  $S_{\text{tot}}^z = 0$ , in which sector one expects the  $S_{\text{tot}} = N/2$  and  $S_{\text{tot}} = 0$  to have a similar level of entanglement, a key to guaranteeing that the DMRG routine is unbiased and amenable to a reasonable bond dimension. They find a transition from  $S_{\text{tot}} = N/2$  to  $S_{\text{tot}} = 0$  around  $t' = t'_c$ , as shown in Figure 1.7.

They also calculate the nearest-neighbor correlation function  $(\mathbf{S} \cdot \mathbf{S})_{n.n.}$ , aver-

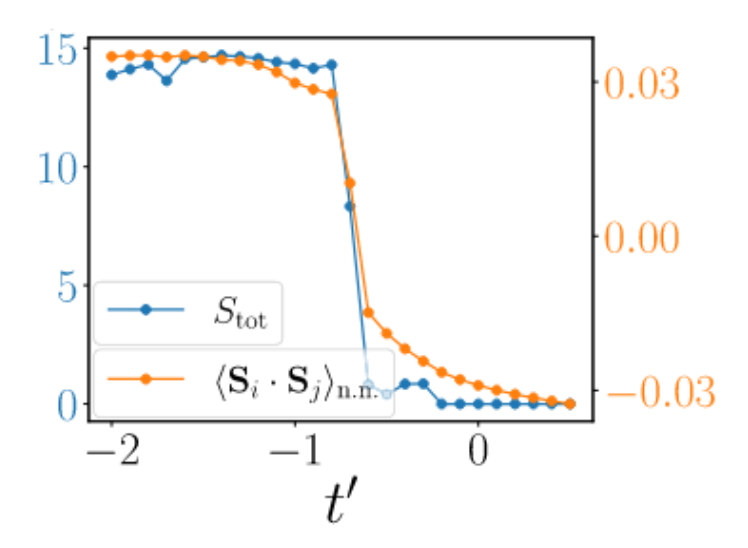


**Figure 1.7.** The total spin  $S_{tot}$  and nearest-neighbor correlation function  $\langle \mathbf{S} \cdot \mathbf{S} \rangle_{n.n.}$  of the ground state calculated by the DMRG method for N=30 particles in a  $4 \times 20$  strip. Here,  $S_{tot,max} = N/2 = 15$ .

aged over all bonds of the square lattice. They find clear evidence of ferromagnetic to antiferromagnetic correlations, as shown in Figure 1.8(b). The same calculation is carried out for a wide range of n and t', and the results are collected in Figure 1.8(c)–2(f). Here, for better comparison and visualization the results are normalized by  $S_{\text{tot,max}} = N/2$  and N for Figure 1.8(c)-(f), respectively.

A notable feature in Figure 1.8(c)–(f) is that for all calculations,  $t'_c$  approaches -0.5 at the low-density limit when  $n \to 0$ . They call the ferromagnetism emerged in this regime as the Müller-Hartmann mechanism. In this regime, the general trend is that  $t'_c$  decreases as n increases.

Nearby half filling with n=1, it is known that hole doping can result in Nagaoka ferromagnetism at infinite U. Strictly speaking, Nagaoka ferromagnetism can only be proved for single-hole doping with t'<0. But their numerical results show that when t'=0, the Nagaoka ferromagnetism can exist up to  $\sim 20\%$  of hole doping, that is, for  $0.8 \lesssim n < 1$ . They say this is consistent with previous numerical results[38]. Hence, they attribute the ferromagnetism nearby half filling as the Nagaoka mechanism.

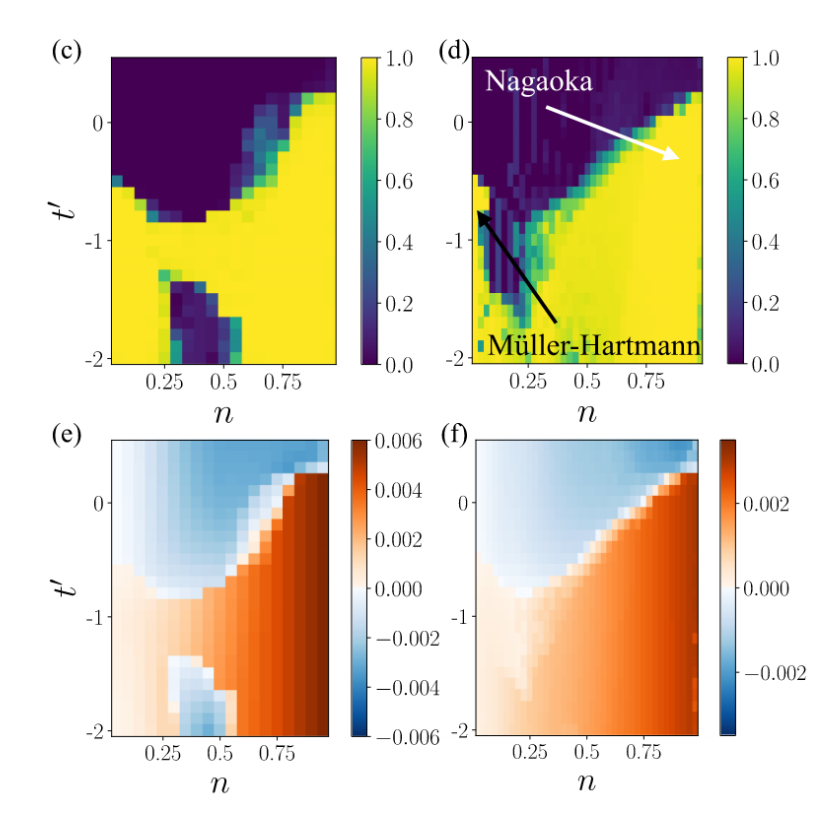


**Figure 1.8.** (c), (d) The total spin  $S_{tot}$  as a function of n and t', normalized by the maximum total spin of the filling  $S_{tot,max} = N/2$ , for (c)  $2 \times 20$  and (d)  $4 \times 20$  strips, respectively. (e), (f) The nearest-neighbor correlation function  $\langle \mathbf{S} \cdot \mathbf{S} \rangle_{n.n.}$  as a function of n and t', normalized by the particle number N, for  $2 \times 20$  and  $4 \times 20$  strips, respectively.

### 1.4 Further recent experimental works

Recent advancements in ferromagnetism research, particularly within frustrated lattice systems, have unveiled novel magnetic behaviors and promising applications, paving the way for innovations in spintronics, quantum computing, and next-generation storage technologies. This summary outlines the progress in general ferromagnetism studies and specific experimental developments in frustrated lattices.

In the realm of ferromagnetism, significant breakthroughs have been reported in 2024–2025. The discovery of "altermagnetism," a third class of magnetism, has been experimentally imaged for the first time, demonstrating its potential to bridge conventional ferromagnetic and antiferromagnetic properties, which could revolutionize digital memory technologies [39]. Researchers at MIT have demonstrated a novel form of ferromagnetism enabling low-power spintronic memory, highlighting its efficiency for future applications[7]. Additionally, two-dimensional metalorganic ferromagnets, such as Ni-TCNE, exhibit ordered ferromagnetic behavior, offering new avenues for designing 2D magnetic materials[40]. High-magnetic-field studies have further underscored the critical role of ferromagnetic materials in medical and energy applications[41]. These findings indicate a rapid transition from fundamental exploration to practical technological advancements in ferromagnetism research.

In frustrated lattice systems, geometric frustration—arising from competing magnetic interactions in structures like kagome, triangular, or honeycomb lattices—has led to emergent phenomena, including spin liquids and unexpected ferromagnetic order. Experimental efforts have focused on tuning frustration and observing novel magnetic phases. In kagome lattices, studies on monolayer Mn breathing kagome lattices revealed triple-Q magnetic states and flat-band-induced ferromagnetic instabilities, underscoring the pivotal role of orbital selectivity in magnetic control[42]. By applying anisotropic strain, researchers finely tuned frustration in organic quantum kagome lattices, successfully inducing ferromagnetic phases [43]. Moreover, kagome ferromagnets exhibited pronounced room-temperature anomalous Hall and Nernst effects, expanding the family of topological magnetic materials [44]. Other experiments confirmed field-induced ferro-

magnetism through isothermal magnetization measurements, with non-saturated characteristics attributed to residual frustration. Compounds with Archimedean lattices displayed exotic frustrated magnetism, providing a new platform for quantum magnetism studies.

In itinerant fermion systems, local frustration shaped magnetic order, with odd-numbered rings suppressing ferromagnetism[45]. Furthermore, stress experiments demonstrated that applied pressure can alleviate frustration, driving a phase transition from antiferromagnetic to ferromagnetic states. In three-dimensional frustrated systems, magnetic nanowire lattices, fabricated via nanoprinting and characterized through magnetic imaging, revealed spin textures and domain wall propagation, establishing a new paradigm for artificial frustrated systems[46].

These experimental studies extensively employed techniques such as powder neutron diffraction, and magnetization measurements, confirming that emergent ferromagnetism in frustrated lattices stems from competing interactions and external tuning (e.g., strain or pressure). Looking forward, integrating altermagnetism with frustrated systems holds promise for further advancing quantum magnetism and topological magnetic materials, providing both theoretical and experimental foundations for the design of next-generation magnetic devices.

# Chapter 2

# Theoretical approach to ferromagnetism in frustrated lattice

This chapter establishes the theoretical framework for studying magnetic properties in frustrated lattice systems using the T-matrix approximation. First we introduce T-matrix approximation[18, 47, 48], which captures correlation effects through the resummation of repeated scattering processes between electrons and applies this theoretical framework to finite-size clusters, providing the computational scheme for calculating ground-state energies and determining magnetic phase boundaries. And we also introduce using T-matrix approximation to analysis the ferromagnetism in iron-series metals[49]. Then we extends the formulation to the thermodynamic limit, where discrete momentum sums are replaced by Brillouin zone integrations, enabling the study of bulk properties and phase transitions. Fially, we introduces two specific lattice models with different hopping directions that will be analyzed using the developed T-matrix methodology.

## 2.1 T-matrix approximation

This section develops the theoretical framework to calculate the paramagnetic energy in the Hubbard model. In Sec. 2.1, we introduce the two-electron Hamilto-

nian and evaluate the interaction energy at the Hartree–Fock level as a baseline. In Sec. 2.2, we go beyond mean-field by applying the T-matrix approximation, which resums repeated scattering processes to capture correlation effects more accurately.

# 2.1.1 Two-electron Hamiltonian and Hartree–Fock approximation

In this section, we set up the two-electron problem that forms the basis of our discussion. Starting from the Hubbard Hamiltonian, we restrict ourselves to the case of two electrons interacting via an on-site Coulomb repulsion. The corresponding wave functions are expressed in terms of Bloch states, which are connected to the localized Wannier basis through standard Fourier relations. Within this framework, the interaction matrix elements reduce to the local term U, identified with the Coulomb self-energy of an atomic orbital. As a first step, we evaluate the interaction energy in the Hartree–Fock approximation, which provides a simple reference point by accounting only for single scattering processes between electrons. This yields the well-known expression for the energy shift depending on the relative spin orientation of the particles.

To set up the formalism, we first discuss the multiple scattering between two electrons in the absence of other electrons. The Hamiltonian governing the motion of two electrons is represented by

$$H = H_0(1) + H_0(2) + V(1, 2), (2.1)$$

where 1 and 2 denote the coordinates of electrons 1 and 2, respectively,  $H_0$  is the one electron energy, V(1,2) the interaction between two electrons. The eigenvalue of  $H_0$  associated with a given wave vector k is denoted by  $\varepsilon(k)$ . The corresponding wave function  $\varphi(x,k)$  with x=1 or 2 is connected to the Wannier function associated with a given lattice site R, W(x,R), by the well-known relations,

$$\varphi(x,k) = (1/\Omega)^{1/2} \sum_{R} W(x,R) \exp(ik \cdot R)$$
 (2.2)

and

$$W(x,R) = (1/\Omega)^{1/2} \sum_{k} \varphi(x,k) \exp(-ik \cdot R), \qquad (2.3)$$

where  $\Omega$  is the number of the lattice sites in a given volume. The matrix elements of V(1,2) referred to the Wannier functions are assumed to be

$$\int W^*(1,R_1)W^*(2,R_2)V(1,2)W(1,R_3)W(2,R_4)dv_1dv_2 = U\delta_{R_1,R_2}\delta_{R_2,R_3}\delta_{R_3,R_4},$$
(2.4)

where U is non-zero only when all four coordinates refer to the same lattice site, i.e.,  $R_1 = R_2 = R_3 = R_4$ . The parameter U defined by Eq.2.4 is identified with the Coulomb self-energy of the atomic orbital. The matrix elements of V(1,2) referred to  $\varphi$ 's are easily calculated by the use of Eq.2.2 and 2.4 to be

$$\int \varphi^*(1, \boldsymbol{k}_1) \varphi^*(2, \boldsymbol{k}_2) V(1, 2) \varphi(1, \boldsymbol{k}_3) \varphi(2, \boldsymbol{k}_4) d\nu_1 d\nu_2 = (U/\Omega) \delta(\boldsymbol{k}_1, \boldsymbol{k}_2; \boldsymbol{k}_3, \boldsymbol{k}_4) \quad (2.5)$$

with

$$\delta(\mathbf{k}_1, \mathbf{k}_2; \mathbf{k}_3, \mathbf{k}_4) = \begin{cases} 1 & \text{if } \mathbf{k}_1 + \mathbf{k}_2 = \mathbf{k}_3 + \mathbf{k}_4 + \mathbf{K}, \\ 0 & \text{otherwise,} \end{cases}$$
(2.6)

where K represents a reciprocal lattice vector. Let  $|\mathbf{k}_1\sigma_1, \mathbf{k}_2\sigma_2\rangle$  be the antisymmetrized wave function of the state where the one electron states specified by  $\mathbf{k}_1$  with the spin coordinate  $\sigma_1$  and  $\mathbf{k}_2$  with  $\sigma_2$  are occupied. In the Hartree-Fock approximation, the interaction energy of two electrons in this state is given by

$$\Delta E_{HF}(\mathbf{k}_1 \sigma_1, \mathbf{k}_2 \sigma_2) = (U/\Omega)(1 - \delta_{\sigma_1 \sigma_2}), \qquad (2.7)$$

where  $\delta_{\sigma_1\sigma_2} = 1$  for parallel spins  $(\sigma_1 = \sigma_2)$ , and  $\delta_{\sigma_1\sigma_2} = 0$  for antiparallel spins  $(\sigma_1 \neq \sigma_2)$ . This result embodies the effect of the Pauli exclusion principle: parallel spins experience no interaction energy due to exchange effects, while antiparallel spins can occupy the same orbital state and thus experience the full Coulomb repulsion energy  $U/\Omega$ .

# 2.1.2 T-matrix approximation for the paramagnetic energy

The Hartree–Fock result represents only a first-order treatment of the interaction, since it neglects the possibility of repeated scattering between electrons. To obtain a more accurate description of the paramagnetic state, we now employ the T-matrix approximation (TMA). This approach resums the particle-particle ladder series, which collect all possible repeated scattering processes on two electrons, and can therefore be interpreted as a generalized scattering amplitude in the medium. Physically, the T-matrix describes repeated scattering on two electrons, while incorporating the effect of the surrounding Fermi sea by restricting intermediate states to those above the Fermi level, while the presence of other electrons enters self-consistently through the renormalized one-particle spectrum. As a result, the T-matrix provides an effective interaction on two electrons that interpolates smoothly between weak and strong coupling and serves as the foundation for computing the paramagnetic energy.

For parallel spins, the Pauli exclusion principle prevents the electrons from scattering into occupied states, so the Hartree-Fock result remains exact:  $\Delta E = 0$ . The interesting physics arises for antiparallel spins, where repeated scattering processes can occur. In this case, the eigenfunction of H takes the form

$$\Psi(\mathbf{k}_1, \mathbf{k}_2) = |\mathbf{k}_1, \mathbf{k}_2\rangle + (1/\Omega) \sum_{\mathbf{k}_3, \mathbf{k}_4} \Gamma_{\mathbf{k}_3 \mathbf{k}_4} |\mathbf{k}_3, \mathbf{k}_4\rangle \delta(\mathbf{k}_1, \mathbf{k}_2; \mathbf{k}_3, \mathbf{k}_4), \qquad (2.8)$$

where the spin indices are omitted for simplicity since we consider only antiparallel spin pairs. Inserting this expression into the Schrödinger equation  $H\Psi = E\Psi$  [18].Here  $H = H_0 + V$ , where  $H_0$  denotes the single-particle part acting on two-particle basis states as  $H_0|\mathbf{k}_i,\mathbf{k}_j\rangle = (\varepsilon(\mathbf{k}_i) + \varepsilon(\mathbf{k}_j))|\mathbf{k}_i,\mathbf{k}_j\rangle$ . The contact interaction contributes only for opposite-spin pairs, with matrix elements given by  $\langle \mathbf{k}_a, \mathbf{k}_b | V | \mathbf{k}_c, \mathbf{k}_d \rangle = \frac{U}{\Omega} \delta(\mathbf{k}_a, \mathbf{k}_b; \mathbf{k}_c, \mathbf{k}_d)$ . After inserting and projecting onto  $\langle \mathbf{k}_3, \mathbf{k}_4 |$  yields

$$(\varepsilon_3 + \varepsilon_4 - E) \Gamma_{\mathbf{k}_3 \mathbf{k}_4} + U \delta(\mathbf{k}_1, \mathbf{k}_2; \mathbf{k}_3, \mathbf{k}_4) + \frac{U}{\Omega} \sum_{\mathbf{k}_5, \mathbf{k}_6} \Gamma_{\mathbf{k}_5 \mathbf{k}_6} \delta(\mathbf{k}_5, \mathbf{k}_6; \mathbf{k}_3, \mathbf{k}_4) = 0. \quad (2.9)$$

CHAPTER 2. THEORETICAL APPROACH TO FERROMAGNETISM IN 20 FRUSTRATED LATTICE

For convenience we introduce the quantity

$$S \equiv 1 + \frac{1}{\Omega} \sum_{\mathbf{k}_5, \mathbf{k}_6} \Gamma_{\mathbf{k}_5, \mathbf{k}_6} \delta(\mathbf{k}_1, \mathbf{k}_2; \mathbf{k}_5, \mathbf{k}_6), \qquad (2.10)$$

which depends only on the initial state  $(\mathbf{k}_1, \mathbf{k}_2)$  and not on the specific intermediate states. The equation above then becomes

$$(\varepsilon_3 + \varepsilon_4 - E) \Gamma_{\mathbf{k}_3 \mathbf{k}_4} + U S = 0, \tag{2.11}$$

leading to

$$\Gamma_{\mathbf{k}_3\mathbf{k}_4} = -\frac{US}{\varepsilon_3 + \varepsilon_4 - E},\tag{2.12}$$

substituting this result back into the definition of S gives the self-consistency condition

$$S = 1 - \frac{US}{\Omega} \sum_{\mathbf{k}_5, \mathbf{k}_6} \frac{\delta(\mathbf{k}_1, \mathbf{k}_2; \mathbf{k}_5, \mathbf{k}_6)}{\varepsilon_5 + \varepsilon_6 - E}.$$
 (2.13)

We thus introduce

$$G(E; \mathbf{k}_1, \mathbf{k}_2) \equiv \frac{1}{\Omega} \sum_{\mathbf{k}_5, \mathbf{k}_6} \frac{\delta(\mathbf{k}_1, \mathbf{k}_2; \mathbf{k}_5, \mathbf{k}_6)}{\varepsilon_5 + \varepsilon_6 - E},$$
(2.14)

so that

$$S = \frac{1}{1 + UG(E; \mathbf{k}_1, \mathbf{k}_2)},$$
(2.15)

the explicit form of  $\Gamma$  is then

$$\Gamma_{\mathbf{k}_3\mathbf{k}_4} = -\frac{U}{1 + U G(E; \mathbf{k}_1, \mathbf{k}_2)} \cdot \frac{1}{\varepsilon(\mathbf{k}_3) + \varepsilon(\mathbf{k}_4) - E}.$$
 (2.16)

Projecting the Schrödinger equation onto the bare state  $\langle \mathbf{k}_1, \mathbf{k}_2 |$  yields the energy eigenvalue

$$E = \varepsilon(\mathbf{k}_1) + \varepsilon(\mathbf{k}_2) + \frac{U}{\Omega}S, \tag{2.17}$$

so that the interaction-induced energy shift is

$$\Delta E(\mathbf{k}_1, \mathbf{k}_2) = E - \left(\varepsilon(\mathbf{k}_1) + \varepsilon(\mathbf{k}_2)\right) = \frac{U/\Omega}{1 + UG(E; \mathbf{k}_1, \mathbf{k}_2)}..$$
 (2.18)

CHAPTER 2. THEORETICAL APPROACH TO FERROMAGNETISM IN 21 FRUSTRATED LATTICE

In Eq.2.14 and 2.16, the energy shift  $\Delta E$  in the denominator is neglected because it is of order  $1/\Omega$  and much smaller than the band energies. Finally, we can determine  $\Gamma$ :

$$\Gamma_{\mathbf{k}_3\mathbf{k}_4} = -\frac{U}{1 + UG(\mathbf{k}_1, \mathbf{k}_2)} \cdot \frac{1}{\varepsilon(\mathbf{k}_3) + \varepsilon(\mathbf{k}_4) - \varepsilon(\mathbf{k}_1) - \varepsilon(\mathbf{k}_2)}$$
(2.19)

Here,  $G(\mathbf{k}_1, \mathbf{k}_2)$  represents the density of intermediate scattering states and characterizes the strength of correlation effects. The factor 1/(1+UG) shows how repeated scattering reduces the effective interaction strength compared to the bare Hartree-Fock result.

Comparing  $\Delta E$  given by Eq.2.18 with  $\Delta E_{HF}$  of Eq.2.7, we can see that the reduction of the interaction energy due to electron correlation is indicated by the factor  $1/(1 + UG(\mathbf{k}_1, \mathbf{k}_2))$ .

To account for the presence of other electrons in the system, we make the following modifications to the above calculation. First, we restrict the states  $k_3$  and  $k_4$  in the sum of Eqs. (2.8) and (2.11) to the unoccupied states above the Fermi level, since the occupied states below the Fermi level are not available for scattering due to the Pauli exclusion principle. Second, we assume that other electrons affect the motion of the interacting pair only through a self-consistently defined potential energy. This potential energy is understood to be included already in the one-electron energy  $H_0$  of Eq.2.1.

We define the self-consistent one-electron energy  $\varepsilon(\mathbf{k})$  by

$$\varepsilon(\mathbf{k}) = \varepsilon_0(\mathbf{k}) + \sum_{\mathbf{k}'} \Delta E(\mathbf{k}, \mathbf{k}'), \qquad (2.20)$$

where  $\varepsilon_0(\mathbf{k})$  is the one-electron energy in the absence of interactions, and the sum in the second term is taken over all occupied states below the Fermi level. It is  $\varepsilon(\mathbf{k})$ , not  $\varepsilon_0(\mathbf{k})$ , that enters into the expressions for  $\Delta E$  and  $G(\mathbf{k}_1, \mathbf{k}_2)$  in Eqs. (2.10) and (2.11). Equation (2.12) represents the self-consistency condition that determines the renormalized single-particle spectrum.

With these modifications, we can define an effective interaction strength in the

paramagnetic state as

$$U_{\text{eff}}(\mathbf{k}_1, \mathbf{k}_2) = \frac{U}{1 + UG(\mathbf{k}_1, \mathbf{k}_2)},$$
 (2.21)

where the sum in Eq.2.14 that defines  $G(\mathbf{k}_1, \mathbf{k}_2)$  is understood to be taken over unoccupied states only. This quantity  $U_{\text{eff}}(\mathbf{k}_1, \mathbf{k}_2)$  is the T-matrix element in the particle-particle channel, which represents the exact scattering amplitude between two electrons in the presence of the filled Fermi sea. Since  $G(\mathbf{k}_1, \mathbf{k}_2)$  is generally of the order of 1/W, where W is the bandwidth, Eq.2.21 yields

$$U_{\text{eff}} \approx W \quad \text{if} \quad U \gg W,$$
 (2.22)

which shows that the effective interaction is limited by the bandwidth in the strong coupling regime, as discussed in the introduction.

For pairs of electrons both occupying states near the bottom of the band (corresponding to points of high symmetry such as  $\mathbf{k} = 0$  or  $\mathbf{k} = \mathbf{K}/2$ ), the function G can be written as

$$G(0,0) = \frac{1}{2} \int_{\varepsilon_E}^{W} \frac{\eta(\varepsilon)}{\varepsilon} d\varepsilon, \qquad (2.23)$$

where  $\eta(\varepsilon)$  is the density of states per unit energy per atom per spin, and  $\varepsilon_F$  is the Fermi energy. The factor of 1/2 accounts for the fact that we sum over pairs of electrons.

For most electron pairs,  $G(\mathbf{k}_1, \mathbf{k}_2)$  does not differ significantly from G(0,0). This is because the scattering process corresponds to s-wave scattering that does not depend strongly on the relative momentum of the interacting pair, and also because the crystal momentum conservation condition in Eq.2.6 typically separates the energies of low-lying excited states from the unperturbed energy by an amount of order  $\varepsilon_F$ . Thus we obtain an approximate estimate of  $U_{\text{eff}}$ :

$$U_{\text{eff}}^0 = \frac{U}{1 + UG(0,0)}. (2.24)$$

The difference between Eq.2.24 and the average of Eq.2.21 over  $\mathbf{k}_1$  and  $\mathbf{k}_2$  below the Fermi level is estimated by numerical calculation to be within 5 percent

CHAPTER 2. THEORETICAL APPROACH TO FERROMAGNETISM IN 23 FRUSTRATED LATTICE

for the case of constant density of states  $\eta = \text{constant}$ .

# 2.2 T-matrix Approach to Ferromagnetism in Iron-Series Metals

To analyze ferromagnetism in the iron-series metals, we employ the t-matrix approach. We focus on the case of two degenerate degenerate d-like bands a and b, where both intra- and inter-orbital Coulomb interactions are relevant. Within this framework, the ground-state singlet and ferromagnetic energies can be expressed as follows [49]:

$$E_0 = N\rho^{5/3} \left\{ \frac{18}{5} W + 2\rho^{1/3} [\tilde{t}_{aa}(\rho) + \tilde{t}_{ab}(\rho) + \tilde{t}_{ab}(\rho)] \right\}.$$
 (2.25)

It is to be compared to the ferromagnetic state, with half the particles in band a and half in band b but all with spin "up," which has energy

$$E_f = N\rho^{5/3} \left[ 2^{2/3} \frac{18}{5} W + 4\rho^{1/3} \tilde{t}_{ab}(2\rho) \right], \qquad (2.26)$$

and with the ferromagnetic state in which all the particles, of spin up, are also in a single band, say a (this represents spin and orbital magnetism, and should occur when the perturbations of the solid are too weak to quench the orbital moments of the individual atoms, as in f shells of the rare earths). This state has energy

$$E_{f,0} = N\rho^{5/3} \left(\frac{9}{5} 4^{5/3} W\right). \tag{2.27}$$

The case of maximal interband exchange j=1 is special, The parameter j is thus the fractional inter-band exchange parameter, 0 < j < 1. We compare the three energies and conclude that Eq.2.27, representing spin + orbital magnetism, can never lie lowest. The phase diagram showing the region where the spin-only magnetic moments form is remarkably similar to Figure 2.1, with only the numerical value of parameters  $\rho_c = 0.04$  and  $U_{\min}/W = 1$  being different. Doubling the number of bands allows magnetic moment formation at much lower densities and

interaction parameter U than previously.

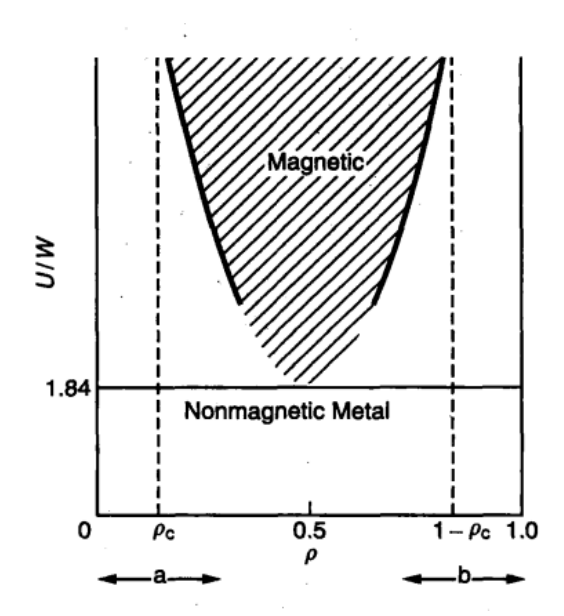


**Figure 2.1.** Phase diagram of 1-band Hubbard model at T = 0, based on low-density theory. Region (a) is low density for electrons and (b) for holes. The high density results near 0.5 are unreliable, due to limitations of the theory. Potentially magnetic region is shaded, and  $\rho_c = 0.136$  in 3D.

Effects of temperature on the phase diagram of the one-band Hubbard model have been examined by N. Berker, in several publications based on quantum Monte Carlo numerical calculations.[50, 51, 52] Figure 2.3 is representative of the results. At various values of U (note that U/t=6 is small, equivalent to U/W=0.5 on the sc lattice) the AF phase that is stable at half-occupancy gives way to a disordered phase at higher temperatures. But most remarkably, new phases, shared here and called the  $\tau$ -phases, appear in the diagram. There is no other theoretical justification for, or description of, the  $\tau$ -phases. These are possibly artifacts of the method. However, the very existence of high-temperature superconductivity should make one reluctant to dismiss these so-far unidentified states.

The physically plausible cases of partial Hund's rule exchange  $j = J_{ab}/U_{ab} < 1$  may be of interest. They compared Eq.2.25 - 2.27 by numerical calculation,[49] assuming  $U_{ab} = \frac{1}{2}U_{aa} \equiv U$ , and found: spin + orbital magnetism never occurs for U/W < 20 nor for densities far from 1/2, so this case may be eliminated from practical considerations even though it is good to know it exists (in principle) in

CHAPTER 2. THEORETICAL APPROACH TO FERROMAGNETISM IN 25 FRUSTRATED LATTICE

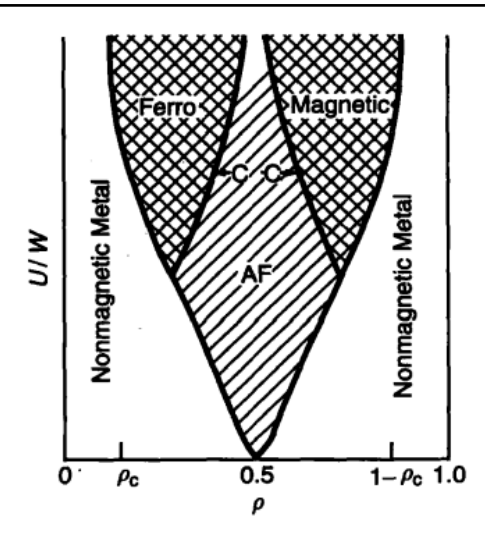


**Figure 2.2.** Same as preceding, with magnetic ordering taken into account. The half-filled band is most easily susceptible to AF ordering (Examples: NiO, and also 1D Hubbard model [53] but at strong enough coupling in 2D or 3D (not 1D) gives way to the ferromagnetic phase (cross-hatching).

the atomic limit  $W \to 0$ . Spin magnetism has itself a restricted range of stability, which depends strongly on j. For j = 0.5 or greater, the situation is qualitatively similar to j = 1, whereas for smaller values of j (0.2 or 0.1) the regions of stability shrink rapidly and become nonexistent at j = 0. Thus, regardless of the strength of the interaction parameter U, the existence of a magnetic moment ultimately depends on the Hund's rule exchange parameter, as a stabilizing factor.

The spatial ordering of the moments, once they are created, is a delicate competition between several mechanisms, principally, the indirect exchange and Nagaoka mechanisms. But before proceeding, it is prudent to consider to what extent electrons in real materials satisfy the various simplifying assumptions, for example, the effective-mass approximation  $E(k) = \hbar^2 k^2/2m$  with  $m = m^*$  the band structure effective mass before interactions and  $= \tilde{m}$  the total mass after the interactions (which are necessarily strong and thus nontrivial) have been incorporated.

The hypothesis of two kinds of d electrons, has been given added credence lately by Stearns. Her "95% local" and "5%" itinerant model counters the pure itinerant or pure Heisenberg models, against which substantial evidence has been accumulating. In her view, [55] most (95%) of the d electrons lie in the relatively

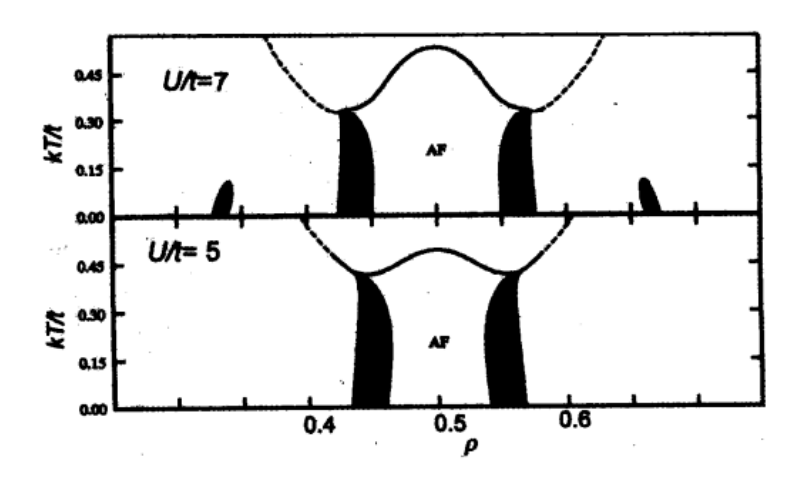
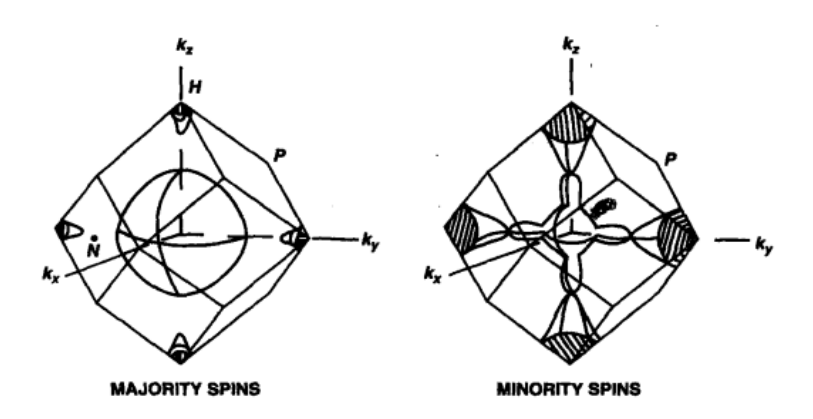


Figure 2.3. Phase diagram at finite T in 3D Hubbard model, near half-filling, for two values of U in weak coupling. Shaded areas represent Berker's  $\tau$ -phase.



**Figure 2.4.** Fermi surface of iron, as given in Gold et al.[54], here adapted from Stearns[55].

CHAPTER 2. THEORETICAL APPROACH TO FERROMAGNETISM IN 27 FRUSTRATED LATTICE

# 2.2. T-MATRIX APPROACH TO FERROMAGNETISM IN IRON-SERIES METALS

flat portions of the band structure, where the high density of states (or small W, large U/W) promotes magnetic moment formation, with the small residual fraction occupying states well described in the effective mass approximation, with effective masses  $\sim m_{\rm el}$ . To see this, let us examine the Hartree-Fock band structure of iron, as shown in Figure 2.4and 2.5 reproduced from her article, "Why is iron magnetic?" [55] There are shown the flat parts of the d bands and the itinerant parts, drawn in heavy lines. The latter have a curvature corresponding to approximately the electron free mass  $m_{\rm el}$ , Fermi wave vectors and occupation numbers  $n\pm$  that have been given as [56, 57]

in agreement with tunneling experiments.

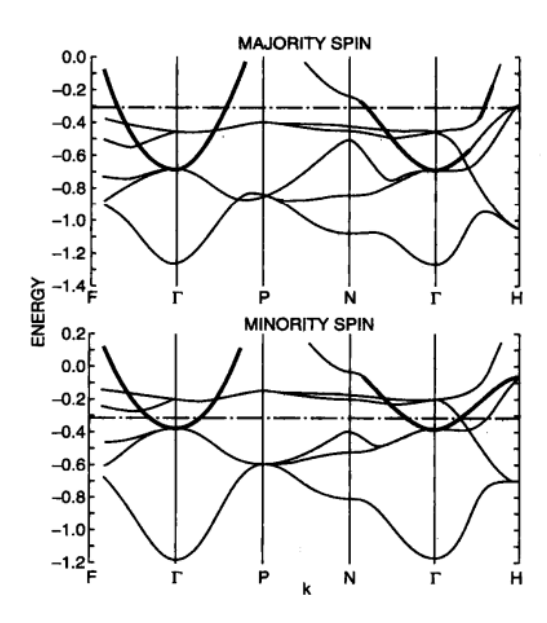


**Figure 2.5.** Band structure of iron, for majority and minority electrons as calculated in Duff and Das[58] and reproduced in Stearns[55].

A plausible explanation combines several effects. The low density of itinerant d electrons together with strong interactions places the system in the ferromagnetic regime of the phase diagram. Moreover, local moments are spatially extended

CHAPTER 2. THEORETICAL APPROACH TO FERROMAGNETISM IN 28 FRUSTRATED LATTICE

rather than point-like, so the indirect exchange is better described by a jellium picture, which ensures ferromagnetism. The only practical procedure is to calculate the Hartree–Fock energy first, as deduced from the band structure (Figure 2.5), and then add the interaction energies as computed from the  $\tilde{t}$ 's, as in the two-band case analyzed above. In practice, this amounts to evaluating the Hartree–Fock band energy and then adding the interaction corrections from the T-matrix, comparing the total energy of different magnetic states. These arguments suggest that iron is indeed stabilized in the ferromagnetic state.

#### 2.3 TMA calculation for Lattices

#### 2.3.1 Finite case

To apply the T-matrix approximation to concrete lattice magnetism calculations, we consider finite clusters with  $\Omega = L \times L$  sites under periodic boundary conditions. We restrict our analysis to electron fillings  $N = N_{\uparrow} + N_{\downarrow}$  where both spin components  $N_{\sigma}$  (with  $\sigma = \uparrow, \downarrow$ ) correspond to closed energy shells, ensuring that finite-size effects are minimized and the results are representative of the thermodynamic limit.

For given values of  $N_{\uparrow}$  and  $N_{\downarrow}$ , we calculate the ground-state energy using the T-matrix expression. The total energy consists of the kinetic energy and the T-matrix contribution from all antiparallel spin pairs:

$$E = \sum_{\mathbf{k},\sigma} f_{\sigma}(\mathbf{k}) \varepsilon_{\mathbf{k}} + \frac{U}{\Omega} \sum_{\mathbf{k},\mathbf{k}'} \frac{f_{\uparrow}(\mathbf{k}) f_{\downarrow}(\mathbf{k}')}{1 + U \chi_{pp}(\mathbf{k} + \mathbf{k}', \overline{\varepsilon}_{\mathbf{k},\uparrow} + \overline{\varepsilon}_{\mathbf{k}',\downarrow})},$$
 (2.28)

where  $f_{\sigma}(\mathbf{k})$  are the occupation numbers for spin- $\sigma$  electrons,  $\varepsilon_{\mathbf{k}}$  is the bare single-particle dispersion, and  $\overline{\varepsilon}_{\mathbf{k},\sigma}$  represents the self-consistently renormalized single-particle energies. The second term directly implements the T-matrix result from Eq.2.21: the denominator  $1 + U\chi_{pp}$  corresponds to our earlier expression  $1 + UG(\mathbf{k}_1, \mathbf{k}_2)$ , while the factors  $f_{\uparrow}(\mathbf{k})f_{\downarrow}(\mathbf{k}')$  ensure that we only sum over occupied pair states.

The particle-particle susceptibility  $\chi_{pp}$  in the denominator is given by:

$$\chi_{pp}(\mathbf{q},\omega) = \frac{1}{\Omega} \sum_{\mathbf{p}} \frac{[1 - f_{\uparrow}(\mathbf{p})][1 - f_{\downarrow}(-\mathbf{p} + \mathbf{q})]}{\overline{\varepsilon}_{\mathbf{p},\uparrow} + \overline{\varepsilon}_{-\mathbf{p}+\mathbf{q},\downarrow} - \omega},$$
(2.29)

which is precisely the finite-temperature generalization of the two-particle Green's function  $G(\mathbf{k}_1, \mathbf{k}_2)$  defined in Eq.2.14. The key correspondence is that  $\chi_{pp}(\mathbf{q}, \omega)$  represents the same physical quantity—the density of available intermediate scattering states—but now formulated for finite systems with discrete momentum states and explicit Fermi-Dirac occupation factors. The factors  $[1 - f_{\sigma}(\mathbf{k})]$  ensure that only unoccupied states contribute to the scattering processes, consistent with the Pauli exclusion principle that was incorporated into our derivation of the T-matrix.

To determine the magnetic ground state, we systematically calculate the groundstate energy E for all possible closed-shell partitions of the total electron number N into spin-up and spin-down components. The paramagnetic state is identified as the configuration that minimizes E with the smallest possible spin polarization  $|N_{\uparrow} - N_{\downarrow}|$ . If this minimum occurs for  $N_{\uparrow} = N_{\downarrow}$ , the system is paramagnetic; otherwise, it exhibits spontaneous magnetization and is ferromagnetic.

This approach allows us to capture the competition between kinetic energy (favoring delocalization) and interaction energy (potentially favoring localization and magnetic order) within the T-matrix framework, providing a systematic way to study the magnetic phase diagram of correlated electron systems.

#### 2.3.2 Thermodynamic limit case

The finite-size cluster approach described in the previous section provides results for small systems, but to understand the bulk properties and thermodynamic behavior, we extend our T-matrix formulation to the thermodynamic limit. In this limit, the discrete momentum sums are replaced by integrals over the Brillouin zone, and the finite-size constraints on closed energy shells are removed.

The transition from finite clusters to the thermodynamic limit involves the

standard replacement:

$$\frac{1}{\Omega} \sum_{\mathbf{k}} \to \int_{\text{BZ}} \frac{d^2 k}{(2\pi)^2},\tag{2.30}$$

where the integration extends over the entire Brillouin zone. This transformation reflects the fact that in an infinite system, momentum becomes a continuous variable, and the density of states in **k**-space is  $(2\pi)^{-2}$  per unit area.

Under this transformation, the particle-particle susceptibility becomes:

$$\chi_{pp}(\mathbf{q},\omega) = \int_{\mathrm{BZ}} \frac{d^2 p}{(2\pi)^2} \frac{[1 - f_{\uparrow}(\mathbf{p})][1 - f_{\downarrow}(-\mathbf{p} + \mathbf{q})]}{\overline{\varepsilon}_{\mathbf{p},\uparrow} + \overline{\varepsilon}_{-\mathbf{p}+\mathbf{q},\downarrow} - \omega},$$
 (2.31)

where the discrete sum over intermediate states has been replaced by a momentum integral. The occupation factors  $f_{\sigma}(\mathbf{k})$  now represent the smooth Fermi-Dirac distribution in the thermodynamic limit, and the energy denominators involve the self-consistently determined quasiparticle energies  $\overline{\varepsilon}_{\mathbf{k},\sigma}$ .

Similarly, the total energy per site in the thermodynamic limit takes the form:

$$e = \int_{BZ} \frac{d^2k}{(2\pi)^2} \sum_{\sigma} f_{\sigma}(\mathbf{k}) \,\varepsilon_{\mathbf{k}} + U \iint_{BZ} \frac{d^2k}{(2\pi)^2} \frac{d^2k'}{(2\pi)^2} \, \frac{f_{\uparrow}(\mathbf{k}) \,f_{\downarrow}(\mathbf{k'})}{1 + U \,\chi_{pp}(\mathbf{k} + \mathbf{k'}, \,\overline{\varepsilon}_{\mathbf{k},\uparrow} + \overline{\varepsilon}_{\mathbf{k'},\downarrow})}.$$
(2.32)

The first term represents the kinetic energy contribution, integrated over all occupied states in the Brillouin zone. The second term captures the T-matrix correction to the interaction energy, now expressed as a double integral over all momentum pairs. This formulation preserves the essential physics of the T-matrix approximation while allowing for the study of bulk properties, phase transitions, and critical phenomena.

The advantage of this continuum formulation is that it enables analytical progress in certain limits and provides a natural framework for studying system properties through the Fermi-Dirac occupation factors. Moreover, it allows for the investigation of instabilities toward various ordered phases by examining the behavior of  $\chi_{pp}$  and the corresponding T-matrix elements as functions of momentum and frequency.

### 2.4 Lattice models and dispersion relations

To investigate the magnetic properties of frustrated lattice systems, we consider two representative tight-binding models on a two-dimensional square lattice. Both models include hopping parameters that introduce geometric frustration and compete with the on-site Coulomb interaction.

### 2.4.1 Two Diagonal Hopping case

First, we consider a tight-binding model on a two-dimensional square lattice that incorporates both nearest-neighbor and next-nearest-neighbor hopping processes. The Hamiltonian for this model is expressed as:

$$H_0 = -t \sum_{\langle i,j\rangle,\sigma} c_{i,\sigma}^{\dagger} c_{j,\sigma} + t' \sum_{\langle \langle i,j\rangle\rangle,\sigma} c_{i,\sigma}^{\dagger} c_{j,\sigma}, \qquad (2.33)$$

where  $c_{i,\sigma}^{\dagger}$  ( $c_{i,\sigma}$ ) denotes the creation (annihilation) operator for an electron with spin  $\sigma$  at site i, t and t' represent the nearest-neighbor and next-nearest-neighbor hopping integrals, respectively. The notation  $\langle i,j \rangle$  indicates nearest-neighbor site pairs, while  $\langle \langle i,j \rangle \rangle$  denotes next-nearest-neighbor site pairs.

To derive the dispersion relation for this model, we employ the standard Fourier transformation method. For a two-dimensional square lattice containing N sites, the Fourier transformation is defined as:

$$c_{i,\sigma} = \frac{1}{\sqrt{N}} \sum_{\mathbf{k}} e^{i\mathbf{k}\cdot\mathbf{r}_i} c_{\mathbf{k},\sigma},$$

$$c_{i,\sigma}^{\dagger} = \frac{1}{\sqrt{N}} \sum_{\mathbf{k}} e^{-i\mathbf{k}\cdot\mathbf{r}_i} c_{\mathbf{k},\sigma}^{\dagger},$$
(2.34)

where  $\mathbf{k} = (k_x, k_y)$  is the wave vector and  $\mathbf{r}_i$  represents the position vector of site i.

For the nearest-neighbor term in a two-dimensional square lattice, each site possesses four nearest neighbors located at  $\mathbf{r}_i + \hat{\mathbf{x}}$ ,  $\mathbf{r}_i - \hat{\mathbf{x}}$ ,  $\mathbf{r}_i + \hat{\mathbf{y}}$ , and  $\mathbf{r}_i - \hat{\mathbf{y}}$ . Here we set the lattice spacing a=1 here and later in this thesis. The nearest-neighbor

hopping term can be written as:

$$-t\sum_{\langle i,j\rangle,\sigma} c_{i,\sigma}^{\dagger} c_{j,\sigma} = -t\sum_{i,\sigma} \left[ c_{i,\sigma}^{\dagger} c_{i+\hat{\mathbf{x}},\sigma} + c_{i,\sigma}^{\dagger} c_{i-\hat{\mathbf{x}},\sigma} + c_{i,\sigma}^{\dagger} c_{i+\hat{\mathbf{y}},\sigma} + c_{i,\sigma}^{\dagger} c_{i-\hat{\mathbf{y}},\sigma} \right]. \quad (2.35)$$

Substituting the Fourier transformation and utilizing the relations  $\mathbf{k} \cdot (\mathbf{r}_i \pm \hat{\mathbf{x}}) = \mathbf{k} \cdot \mathbf{r}_i \pm k_x$  and  $\mathbf{k} \cdot (\mathbf{r}_i \pm \hat{\mathbf{y}}) = \mathbf{k} \cdot \mathbf{r}_i \pm k_y$ , we obtain:

$$-t \sum_{\langle i,j\rangle,\sigma} c_{i,\sigma}^{\dagger} c_{j,\sigma} = -t \sum_{\mathbf{k},\sigma} c_{\mathbf{k},\sigma}^{\dagger} c_{\mathbf{k},\sigma} \left[ e^{ik_x} + e^{-ik_x} + e^{ik_y} + e^{-ik_y} \right]$$

$$= -2t \sum_{\mathbf{k},\sigma} c_{\mathbf{k},\sigma}^{\dagger} c_{\mathbf{k},\sigma} \left[ \cos k_x + \cos k_y \right].$$
(2.36)

The next-nearest-neighbor sites are positioned at  $\mathbf{r}_i + \hat{\mathbf{x}} + \hat{\mathbf{y}}$ ,  $\mathbf{r}_i + \hat{\mathbf{x}} - \hat{\mathbf{y}}$ ,  $\mathbf{r}_i - \hat{\mathbf{x}} + \hat{\mathbf{y}}$ , and  $\mathbf{r}_i - \hat{\mathbf{x}} - \hat{\mathbf{y}}$ . The next-nearest-neighbor hopping term is expressed as:

$$t' \sum_{\langle \langle i,j \rangle \rangle, \sigma} c_{i,\sigma}^{\dagger} c_{j,\sigma}$$

$$= t' \sum_{i,\sigma} \left[ c_{i,\sigma}^{\dagger} c_{i+\hat{\mathbf{x}}+\hat{\mathbf{y}},\sigma} + c_{i,\sigma}^{\dagger} c_{i+\hat{\mathbf{x}}-\hat{\mathbf{y}},\sigma} + c_{i,\sigma}^{\dagger} c_{i-\hat{\mathbf{x}}+\hat{\mathbf{y}},\sigma} + c_{i,\sigma}^{\dagger} c_{i-\hat{\mathbf{x}}-\hat{\mathbf{y}},\sigma} \right].$$
(2.37)

Performing the Fourier transformation, and noting that  $\mathbf{k} \cdot (\mathbf{r}_i \pm \hat{\mathbf{x}} \pm \hat{\mathbf{y}}) = \mathbf{k} \cdot \mathbf{r}_i \pm k_x \pm k_y$ :

$$t' \sum_{\langle \langle i,j \rangle \rangle, \sigma} c_{i,\sigma}^{\dagger} c_{j,\sigma} = t' \sum_{\mathbf{k},\sigma} c_{\mathbf{k},\sigma}^{\dagger} c_{\mathbf{k},\sigma} \left[ e^{ik_x} + e^{-ik_x} \right] \left[ e^{ik_y} + e^{-ik_y} \right]$$

$$= 4t' \sum_{\mathbf{k},\sigma} c_{\mathbf{k},\sigma}^{\dagger} c_{\mathbf{k},\sigma} \cos k_x \cos k_y.$$
(2.38)

Finally, we can get the dispersion for this model:

$$\varepsilon_1(\mathbf{k}) = -2t\left(\cos k_x + \cos k_y\right) + 4t'\cos k_x\cos k_y. \tag{2.39}$$

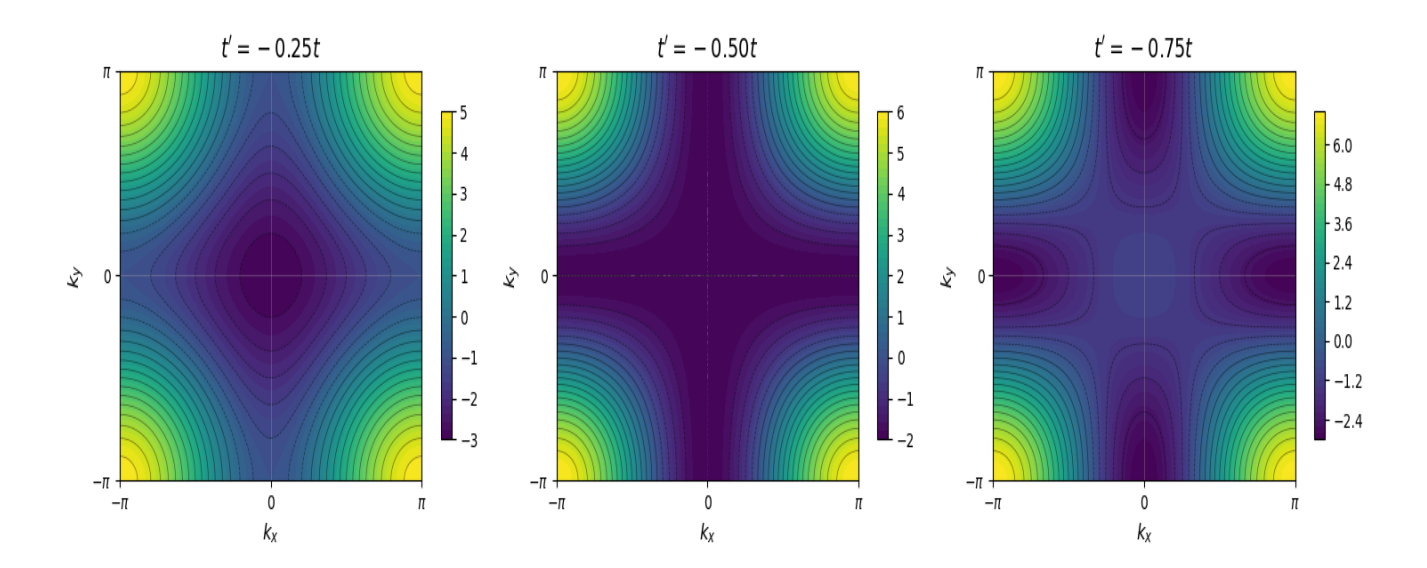


**Figure 2.6.** Two hopping case: Heat map of dispersion within the 1st BZ for three different values of t'/t. t'/t = -0.25, t'/t = -0.5, t'/t = -0.75

As shown in Figure 2.6, when t'/t > -0.5, the band dispersion has a unique minimum at kx,ky = 0. However, when t'/t < -0.5, the band dispersion displays several degenerate minima along kx,ky axes.

### 2.4.2 One Diagonal Hopping case

The second model incorporates nearest-neighbor hopping along with diagonal hopping in a specific direction as shown in Figure 2.7. The corresponding Hamiltonian reads:

$$H_0 = -t \sum_{\langle ij \rangle \sigma} \hat{c}^{\dagger}_{i\sigma} \hat{c}_{j\sigma} - t' \sum_{\langle \langle ij \swarrow \rangle \rangle \sigma} \hat{c}^{\dagger}_{i\sigma} \hat{c}_{j\sigma}, \qquad (2.40)$$

The hopping between the nearest neighbor  $\langle ij \rangle$  is denoted by t, and between the next-nearest neighbor along the dashed line direction  $\langle\langle ij \checkmark \rangle\rangle\rangle$  is denoted by t'. Both t and t' are positive. The next-nearest hopping along another diagonal direction is negligible.

The treatment of the nearest-neighbor term remains identical to that in the

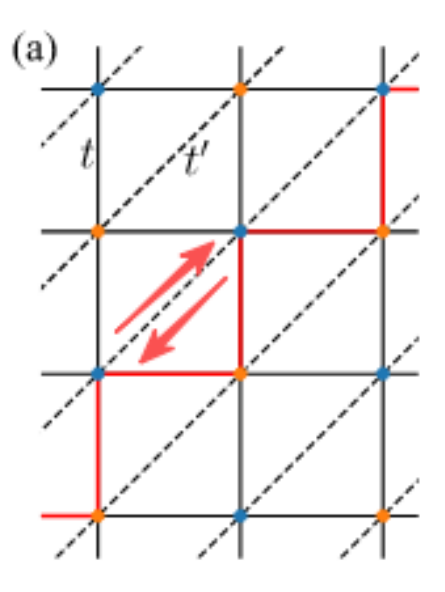


Figure 2.7. The lattice with next-nearest hopping along a specific diagonal direction.

first model, yielding:

$$-t\sum_{\langle i,j\rangle,\sigma} c_{i,\sigma}^{\dagger} c_{j,\sigma} = -2t\sum_{\mathbf{k},\sigma} c_{\mathbf{k},\sigma}^{\dagger} c_{\mathbf{k},\sigma} \left[\cos k_x + \cos k_y\right]. \tag{2.41}$$

In this case, the next-nearest-neighbor sites are positioned at  $\mathbf{r}_i + \hat{\mathbf{x}} + \hat{\mathbf{y}}$ ,  $\mathbf{r}_i - \hat{\mathbf{x}} - \hat{\mathbf{y}}$ . So the diagonal hopping term can write as:

$$t' \sum_{i,\sigma} \left( c_{i,\sigma}^{\dagger} c_{i+\hat{\mathbf{x}}+\hat{\mathbf{y}},\sigma} + \text{h.c.} \right) = t' \sum_{i,\sigma} \left( c_{i,\sigma}^{\dagger} c_{i+\hat{\mathbf{x}}+\hat{\mathbf{y}},\sigma} + c_{i+\hat{\mathbf{x}}+\hat{\mathbf{y}},\sigma}^{\dagger} c_{i,\sigma} \right). \tag{2.42}$$

Upon applying the Fourier transformation:

$$t' \sum_{i,\sigma} \left( c_{i,\sigma}^{\dagger} c_{i+\hat{\mathbf{x}}+\hat{\mathbf{y}},\sigma} + c_{i+\hat{\mathbf{x}}+\hat{\mathbf{y}},\sigma}^{\dagger} c_{i,\sigma} \right) = t' \sum_{\mathbf{k},\sigma} c_{\mathbf{k},\sigma}^{\dagger} c_{\mathbf{k},\sigma} \left[ e^{i(k_x + k_y)} + e^{-i(k_x + k_y)} \right]$$

$$= 2t' \sum_{\mathbf{k},\sigma} c_{\mathbf{k},\sigma}^{\dagger} c_{\mathbf{k},\sigma} \cos(k_x + k_y).$$
(2.43)

The dispersion relation for this model is given by:

$$\varepsilon_2(\mathbf{k}) = -2t(\cos k_x + \cos k_y) + 2t'\cos(k_x + k_y) = -4t\cos(k_+)\cos(k_-) - 2t'\cos(2k_+),$$
(2.44)

where  $k_{\pm} = (k_x \pm k_y)/2$ . It is easy to see that the dispersion minimum occurs at  $k_{-} = 0$ .

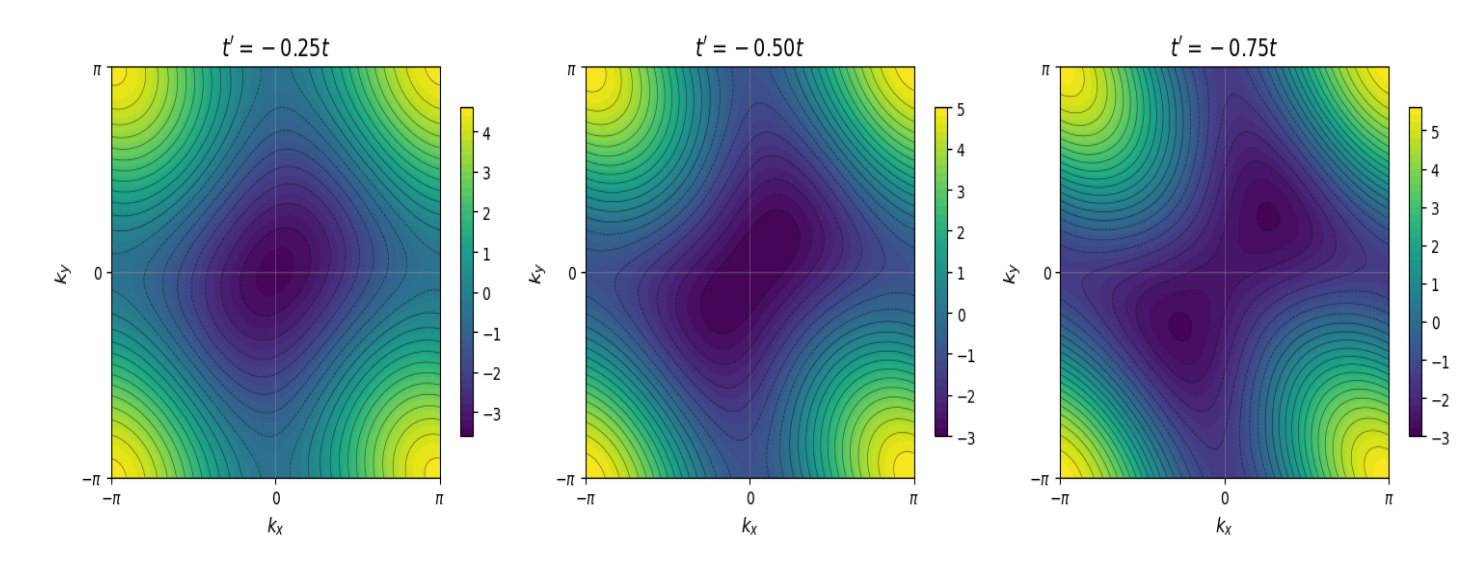


**Figure 2.8.** One hopping case: Heat map of dispersion within the 1st BZ for three different values of t'/t. t'/t = -0.25, t'/t = -0.5, t'/t = -0.75

As shown in Figure 2.8, when t'/t > -0.5, the band dispersion has a unique minimum at  $k_+ = 0$ . However, when t'/t < -0.5, the band dispersion displays two degenerate minima along  $k_+$  axes.

Both models exhibit different degrees of geometric frustration depending on the ratio t'/t. The next-nearest-neighbor hopping in the first model creates frustration by competing with the nearest-neighbor terms, while the diagonal hopping in the second model introduces anisotropic frustration effects. These different geometries allow us to explore how lattice structure affects the competition between kinetic energy and magnetic correlations within the T-matrix framework.

For our numerical calculations, we will examine the magnetic phase diagrams of these models as functions of the interaction strength U/t and the frustration

CHAPTER 2. THEORETICAL APPROACH TO FERROMAGNETISM IN 36 FRUSTRATED LATTICE

2.4. LATTICE MODELS AND DISPERSION RELATIONS							
aramete	r +1 /+						
ar arricuci	1 0 / 0.						
	ID 0 =====	EORETICA		1 011 = 0			

# Chapter 3

# **Numerical Methods**

This chapter presents the numerical study of low-density ferromagnetism in the square-to-triangular lattice, based on the energy comparison method [59, 60, 61] applied to the Hubbard model, together with Python-based computations [62, 63, 64, 65] of two-dimensional ferromagnetic phase diagrams. Initially, we calculate the total energy of the system and determine phase diagrams through numerical integration over finite lattices within a discretized momentum space framework. The approach is then extended to continuous momentum integration in the thermodynamic limit, to better understand the properties of different lattices. These two methodologies complement each other: the former facilitates intuitive verification and cross-validation, while the latter provides a closer approximation to the continuous limit relevant to experimental conditions.

### 3.1 Structure and parameter

## 3.1.1 Computational Framework and Parameter Settings

We employ two distinct computational frameworks to investigate the phase diagram of the two-dimensional Hubbard model: the finite lattice discretization method and the continuous limit method. These two approaches exhibit different characteristics in handling momentum integrals and finite-size effects, providing mutual validation.

In finite lattice calculations, we adopt a discretization scheme with  $L \times L$  twodimensional square lattice points, where the total number of lattice sites is  $\Omega = L^2$ . For lattice size L we choose a favorable balance between computational accuracy and efficiency. The fundamental physical parameters of the system include the hopping energy t, set as the energy unit (t = 1.0), the next-nearest-neighbor hopping parameter t', and the interaction strength U. The interaction strength ranges cover different physical regimes from weak to strong coupling.

In thermodynamic limit calculations, the system is freed from finite-size effects and no longer explicitly depends on the lattice number L. Instead, we directly sample within the continuous first Brillouin zone  $[0, 2\pi] \times [0, 2\pi]$ . This approach can more accurately describe the physical properties of truly infinite systems but requires integration methods to handle continuous integrals. Here we employ the Monte Carlo method and this method is discussed in Appendix I.

In the finite lattice case, we construct a uniform grid discretization of momentum space. We generate equally spaced momentum points by defining  $k_{\text{vals}} = \text{linspace}(0, 2\pi, L)$  and then use a meshgrid procedure to build the complete two-dimensional k-point grid. All k-point information is pre-calculated and stored in array format, which significantly enhances the efficiency of subsequent calculations. To ensure momentum conservation during pair function evaluations, we establish a lookup table mechanism that rapidly identifies k-point pairs.

In the continuous limit method, the momentum space treatment covers the entire first Brillouin zone. The advantage of this method lies in its freedom from discrete grid constraints, enabling a more precise representation of integrals.

# 3.2 Energy Spectrum and Fermi Distribution

### 3.2.1 Dispersion Relations

The system employs a tight-binding model to describe the kinetic energy part of electrons, with the dispersion relations already discussed in Section 2.3 Eq.2.39 and Eq.2.44. These two expressions include the nearest-neighbor hopping term (first term) and the next-nearest-neighbor hopping term (second term), where t' controls the degree of anisotropy in the band structure. When t' = 0, the system reduces

to a simple square lattice tight-binding model; when  $t' \neq 0$ , next-nearest-neighbor hopping introduces complex structural changes in the Fermi surface.

In the finite lattice method, we compute dispersion relations simultaneously for all k-points using optimized vectorized routines, which avoids the inefficiency of explicit loop evaluations. To improve performance, we rely on just-in-time compilation techniques that achieve speeds comparable to C language implementations. Since the band structure remains unchanged for fixed t' parameters, we store the calculated dispersion relations for reuse.

In the continuous limit method, we evaluate dispersion relations for each sampled k-point. Vectorized operations ensure high computational efficiency even when a large number of points are used. To guarantee reproducibility of results, especially important for debugging and validation, we fix random seeds in the sampling process.

### 3.2.2 Energy Sorting and Lookup Tables

An important feature of the finite lattice method is the sorting of eigenvalues. We determine the sorting indices from low to high energy, which then serve as the basis for subsequent Fermi distribution calculations. At the same time, we establish a lookup table mapping k-space coordinates to their sorted indices, which allows rapid access to the energy ordering of any k-point during pair function evaluations. To properly account for periodic boundary conditions in the Brillouin zone, we implement modular arithmetic in the lookup table construction.

The use of lookup tables significantly improves computational efficiency, particularly in interaction energy calculations requiring frequent searches for k-point correspondences. By relying on pre-computation and caching mechanisms [66], we avoid repetitive searches. The cache mechanism is a method that accelerates program execution by temporarily storing calculation results. In computing, when encountering parts that require repeated calculations, the cache mechanism can avoid re-executing these calculations and directly return the previously stored results, thereby improving efficiency. We further employ LRU caching strategies [66] to optimize memory usage, which allows us to directly reuse sorting results and lookup tables for identical t' parameters.

In contrast, the Monte Carlo method does not require explicit energy sorting and lookup tables, since each calculation is based on a fresh set of random sampling points. This makes the Monte Carlo approach better suited for continuous space integrals. Although it forgoes the efficiency of pre-sorting, it gains scalability and provides a closer approximation to the thermodynamic limit.

### 3.2.3 Zero-Temperature Fermi Distribution

The determination of the Fermi distribution in the zero-temperature limit is a core component of the computational framework. Given electron density n, we determine the corresponding chemical potential  $\mu$  numerically so that the total particle number constraint of the system is satisfied.

In the finite lattice method, we exploit the advantage of energy sorting to determine the chemical potential directly from the number of occupied energy levels. For a target density n, the number of electrons to be filled is round( $n \times \Omega$ ), and the corresponding chemical potential is located between the N-th and (N+1)-th energy levels. We take the average of these two levels to ensure numerical stability. This strategy provides both precision and efficiency, while avoiding the complexity of iterative solutions.

At zero temperature, the Fermi distribution function  $f(\mathbf{k})$  reduces to a step function:  $f(\mathbf{k}) = 1$  when  $\epsilon(\mathbf{k}) \leq \mu$ , and  $f(\mathbf{k}) = 0$  otherwise. In the finite lattice approach, we explicitly construct occupied state lists based on energy ordering. This allows us to sum only over occupied states in subsequent interaction energy calculations, which significantly reduces computational load.

In the continuous method, we determine the chemical potential  $\mu_{\sigma}$  by solving the integral equation

$$\langle f(\epsilon_{\mathbf{k}} - \mu_{\sigma}) \rangle_{\mathbf{k}} = n_{\sigma},$$
 (3.1)

where the brackets denote averaging over the Brillouin zone. To solve this equation, we employ Brent's method as shown in Appendix II, which combines the robustness of bisection with the rapid convergence of the secant method. The search interval  $[\mu_{\min}, \mu_{\max}]$  is chosen based on the minimum and maximum values of the band, with an appropriate tolerance to ensure reliable convergence.

Both methods require careful treatment of boundary cases. When density ap-

proaches 0, the chemical potential must lie below the band bottom, while for densities near 1, it should lie above the band top. Proper handling of these conditions guarantees numerical stability and physical consistency.

## 3.3 Energy Calculation Methods

The total energy of the system consists of two contributions: the free electron energy and the interaction energy,

$$E_{\text{total}} = E_{\text{free}} + E_{\text{int}},$$
 (3.2)

where the free energy term describes the kinetic contribution of non-interacting electrons, and the interaction term accounts for the effects of Coulomb repulsion.

#### 3.3.1 Free Energy Term

The free electron energy is obtained from the summation over single-particle states:

$$E_{\text{free}} = \sum_{\mathbf{k}} f(\mathbf{k}) \epsilon(\mathbf{k}),$$
 (3.3)

where  $f(\mathbf{k})$  is the Fermi distribution function and  $\epsilon(\mathbf{k})$  is the dispersion relation. The way this summation is evaluated differs between the two computational methods.

In the finite lattice method, we perform exact summation over discrete k-points on the grid. The pre-computed energy values and occupation numbers allow us to evaluate the sum efficiently in a vectorized manner, avoiding explicit loops. Contributions from spin-up and spin-down states are calculated separately and then added together, making it possible to capture spin polarization effects when present.

To further reduce computational cost, we restrict the summation to occupied states only. By directly extracting the energy values of occupied k-points, we avoid redundant evaluations for unoccupied states. This strategy is particularly effective at low densities, where most states above the Fermi surface remain empty.

In the continuous approach, we estimate the free energy by Monte Carlo integration. We sample random k-points uniformly within the Brillouin zone and compute the average of the product  $\epsilon(\mathbf{k})f(\mathbf{k})$  over these points. The free energy is then approximated as

$$E_{\text{free}} \approx \langle \epsilon(\mathbf{k}) f(\mathbf{k}) \rangle_{\text{MC}}.$$
 (3.4)

This method provides a natural treatment of the thermodynamic limit and avoids discretization artifacts.

### 3.3.2 Interaction Energy Term

The calculation of the interaction energy term is the most complex part of the framework, as it involves quadruple summations and the evaluation of the pair susceptibility function  $\chi_{pp}$ . According to the T-matrix approximation of the Hubbard model, the interaction energy discussed in Section 2.2 can be written as:

$$E_{\text{int}} = U \sum_{\mathbf{k}, \mathbf{k'}} \frac{f(\mathbf{k}) f(\mathbf{k'})}{1 + U \chi_{pp}(\mathbf{k} + \mathbf{k'})},$$
(3.5)

where  $\chi_{pp}$  is the pair susceptibility function.

The pair susceptibility function  $\chi_{pp}(\mathbf{q})$  is defined as:

$$\chi_{pp}(\mathbf{q}) = \sum_{\mathbf{p}} \frac{[1 - f(\mathbf{p})][1 - f(\mathbf{q} - \mathbf{p})]}{\epsilon(\mathbf{p}) + \epsilon(\mathbf{q} - \mathbf{p}) - 2\mu}.$$
(3.6)

This function is a key physical quantity describing the system's response to pairing fluctuations. The numerator  $[1 - f(\mathbf{p})][1 - f(\mathbf{q} - \mathbf{p})]$  represents the probability that both electrons occupy states above the Fermi surface, while the denominator gives the energy cost of creating such two-particle excitations.

In the finite lattice method, we evaluate  $\chi_{pp}(\mathbf{q})$  by summing over all momentum states  $\mathbf{p}$  in the Brillouin zone. The application of periodic boundary conditions ensures the conservation of momentum. Under such conditions, particles or excitations can cross the boundaries of the lattice, thereby enabling the transfer of momentum in calculations. To avoid divergences we exclude contributions when the denominator becomes smaller than a chosen numerical threshold. The results

are normalized by dividing by the total number of lattice sites  $\Omega$ .

To compute the interaction energy, we sum over all pairs of occupied states  $(\mathbf{k}, \mathbf{k}')$ . For each pair, we determine the corresponding momentum transfer  $\mathbf{q} = \mathbf{k} + \mathbf{k}'$ , evaluate  $\chi_{pp}(\mathbf{q})$ , and then accumulate the interaction contribution according to the formula above. This procedure ensures that only physically relevant occupied states contribute to the interaction energy.

In the continuous approach, we adopt Monte Carlo importance sampling to reduce computational complexity. We randomly generate pairs of momentum points  $(\mathbf{k}_1, \mathbf{k}_2)$  and retain only those that are occupied according to the Fermi distribution. This selective sampling avoids ineffective evaluations for unoccupied states and is particularly efficient in the low-density regime.

For each valid pair, we compute the momentum transfer  $\mathbf{q} = \mathbf{k}_1 + \mathbf{k}_2$  and estimate  $\chi_{pp}(\mathbf{q})$  using independent Monte Carlo sampling over intermediate momentum states  $\mathbf{p}$ . Each sampled  $\mathbf{p}$  contributes a term of the form

$$\frac{(1-f(\mathbf{p}))(1-f(\mathbf{q}-\mathbf{p}))}{\epsilon(\mathbf{p})+\epsilon(\mathbf{q}-\mathbf{p})-2\mu},$$

and the susceptibility is obtained as the average over all sampled **p**. This nested Monte Carlo strategy increases the numerical cost, but it provides a natural and scalable way to evaluate interaction energies in the thermodynamic limit.

### 3.3.3 Numerical Optimizations

To improve computational efficiency and handle large-scale systems, we adopt multi-level numerical optimization strategies for both methods.

For the finite lattice method, the optimization mainly focuses on memory efficiency and vectorized calculations. We use the float32 data type instead of the default float64, reducing memory occupancy by half while maintaining numerical precision. This strategy is particularly important when handling large-size systems (such as  $40 \times 40$  lattices). We further accelerate all key numerical calculations, including dispersion relation evaluations and pair susceptibility function evaluations, through Numba's just-in-time compilation, achieving performance comparable to native C implementations.

We also employ caching mechanisms to reduce redundant computations. Specifically, for identical t' parameters, we compute energy sorting results and lookup tables only once and cache them for reuse. With a cache size of 32, this mechanism accommodates all t' values in typical parameter sweeps and effectively avoids repeated calculations.

When the density n > 0.6, we adopt a sampling strategy to control the computational complexity. When the number of occupied state pairs  $n_{\rm up} \times n_{\rm down}$  exceeds a threshold (i.e.,  $n_{\rm up} \times n_{\rm down} > {\rm max\_pairs}$ ), we randomly select a subset of occupied states for calculation and compensate using a scaling factor. This approximation method significantly reduces the computation time while maintaining physical accuracy, making calculations in the high-density region feasible.

For example, suppose there are 5000 spin-up occupied states and 3000 spin-down occupied states in the system. Directly calculating all possible occupied state pairs would result in  $5000 \times 3000 = 15,000,000$  pairs, which involves an enormous computational load. To reduce the computation, we set the maximum number of pairs to 1000 (i.e., max\_pairs = 1000), then randomly select 31 states from the 5000 spin-up occupied states and 32 states from the 3000 spin-down occupied states. The total number of occupied state pairs is  $31 \times 32 = 992$ , which is much smaller than 15,000,000.

To compensate for the error caused by sampling, we calculate a scaling factor:

scale\_factor = 
$$\frac{5000 \times 3000}{31 \times 32} \approx 4812.9$$

This factor is used to adjust the sampling results, making them close to the calculation results obtained when all occupied states are used. In this way, we greatly improve the computational efficiency in high-density scenarios while ensuring computational accuracy.

# 3.4 Determination of lowest energy phase and Parallel Computing

Phase diagram construction requires systematic determination of magnetic phases at each parameter point in the two-dimensional parameter space (t'/t, n). This

process involves extensive repetitive calculations and careful determination of the phase of lowest energy logic. To ensure computational efficiency and reliable results, we employ dedicated phase determination strategies and parallel computing frameworks in both methods.

It is worth mentioning that for the energy calculation of the ferromagnetic state, we only consider the free energy term. This is because, in the context of low-density ferromagnetism, the electron density never exceeds half-filling. Consequently, one term in the interaction energy expression vanishes due to the structure of the Fermi distribution.

# 3.4.1 Energy Comparison Between Ferromagnetic and Paramagnetic States

The core idea of phase determination is to compare total energies of different spin configurations at the same parameter point. The system can exist in two basic magnetic states: ferromagnetic and paramagnetic. In the ferromagnetic state, all electrons align with the same spin direction, i.e., spin-up electron density is n and spin-down electron density is 0, expressed as  $(n_{\uparrow}, n_{\downarrow}) = (n, 0)$ . In the paramagnetic state, spin-up and spin-down electrons are equally populated, i.e.,  $(n_{\uparrow}, n_{\downarrow}) = (n/2, n/2)$ .

We determine the stable phase by the principle of energy minimization. For given parameters (t'/t, n), we calculate the total energies under the two spin configurations,  $E_{\text{ferro}}$  and  $E_{\text{para}}$ . When  $E_{\text{para}} \geq E_{\text{ferro}}$ , the system favors the ferromagnetic state, which we mark as 1 in the phase diagram; conversely, when  $E_{\text{para}} < E_{\text{ferro}}$ , the system favors the paramagnetic state, marked as 0. This binary marking scheme simplifies visualization of the phase diagram while preserving essential information about phase transition boundaries.

In practice, we first calculate the energy of the ferromagnetic state and then evaluate the paramagnetic state energy for comparison.

### 3.4.2 Phase Determination Strategies

In our calculations we consider the density region 0.01; n; 0.75. This regime is physically the most interesting, as it contains the ferromagnetic-paramagnetic

transition boundary. By carrying out complete two-state energy comparisons here, we ensure accurate phase determination.

For the Monte Carlo method, we rely on simplified strategies. In particular, we handle boundary cases through exception handling: when numerical instabilities occur, we assign the paramagnetic state as the default. While this strategy is coarse, it provides the necessary numerical stability for large-scale parameter sweeps.

Near phase transition boundaries, the energy difference between the two states becomes very small, and numerical errors may destabilize phase determination. To address this issue, we increase calculation precision (for instance, by enlarging Monte Carlo sample sizes) and adopt numerically stable algorithms.

#### 3.4.3 Parallelization Implementation

Phase diagram generation requires repeated calculations across a large number of parameter points in two-dimensional parameter space, making it naturally suited for parallelization. We fully exploit the parallel computing capabilities of modern multi-core processors to accelerate this task.

We implement parallelization using Python's standard multiprocessing library. The framework first detects the available number of CPU cores and then creates a corresponding worker pool. The process pool size is typically set to ensure that the number of processes matches computational needs without overloading system resources.

We distribute tasks using the pool.map function, which automatically segments and assigns parameter lists to worker processes. Each worker process independently evaluates the magnetic phase for a parameter couple (t'/t, n) and returns the corresponding marker. This functional design avoids data-sharing issues and guarantees reproducible results.

For the finite lattice method, we emphasize load balancing, since computational complexity varies across parameter points, particularly when density-dependent strategies are applied. The dynamic scheduling of pool.map ensures that worker processes receive new tasks as soon as they finish current ones, thereby maintaining balanced workload distribution.

For the Monte Carlo method, computational cost is nearly uniform across parameter points, as each calculation involves the same number of random samples. This uniformity ensures that parallelization efficiency approaches the theoretical optimum.

We also carefully manage memory usage in the parallel framework. Each worker requires independent memory to store intermediate results, and excessive processes may strain memory resources. To mitigate this, we limit the process pool size and adopt memory-efficient data structures, such as float32 arrays.

The main process collects and reconstructs the results after parallel computations. The pool.map function returns a list of results that we reshape into a two-dimensional phase diagram array. This reconstruction step ensures correct correspondence between parameter ordering and phase markers.

We evaluate parallelization performance by measuring total runtime and average computation time per point. Ideally, using N processes reduces computation time to 1/N of the original. Although actual performance is influenced by process creation overhead, memory bandwidth limits, and load imbalance, we still achieve substantial acceleration.

The final phase diagram is visualized using the Matplotlib library, where black markers indicate ferromagnetic states and white markers represent paramagnetic states.

# Chapter 4

# Numerical Results and Analysis

This chapter presents the numerical results obtained from the implementation of the variational approach described in Chapter 3. We systematically investigate ferromagnetic phase diagrams by examining two distinct lattice dispersions on both finite lattices and in the thermodynamic limit. The analysis reveals the interplay between interaction strength, lattice geometry, and electron density in stabilizing ferromagnetic order.

### 4.1 Finite Lattice Calculations

## 4.1.1 Two-Diagonal Hopping Case

We first examine the model with the two-diagonal hopping dispersion given in Eq.(2.39). This model does not interpolate between a square lattice and a triangular one. We study it as abenchmark for our calculations against previous calculations by by Hlubina et al. [67] using the same T-matrix approximation. Calculations are performed on a finite lattice with linear size L=40. The phase diagrams are constructed by evaluating the energy difference between ferromagnetic and paramagnetic states across the parameter space.

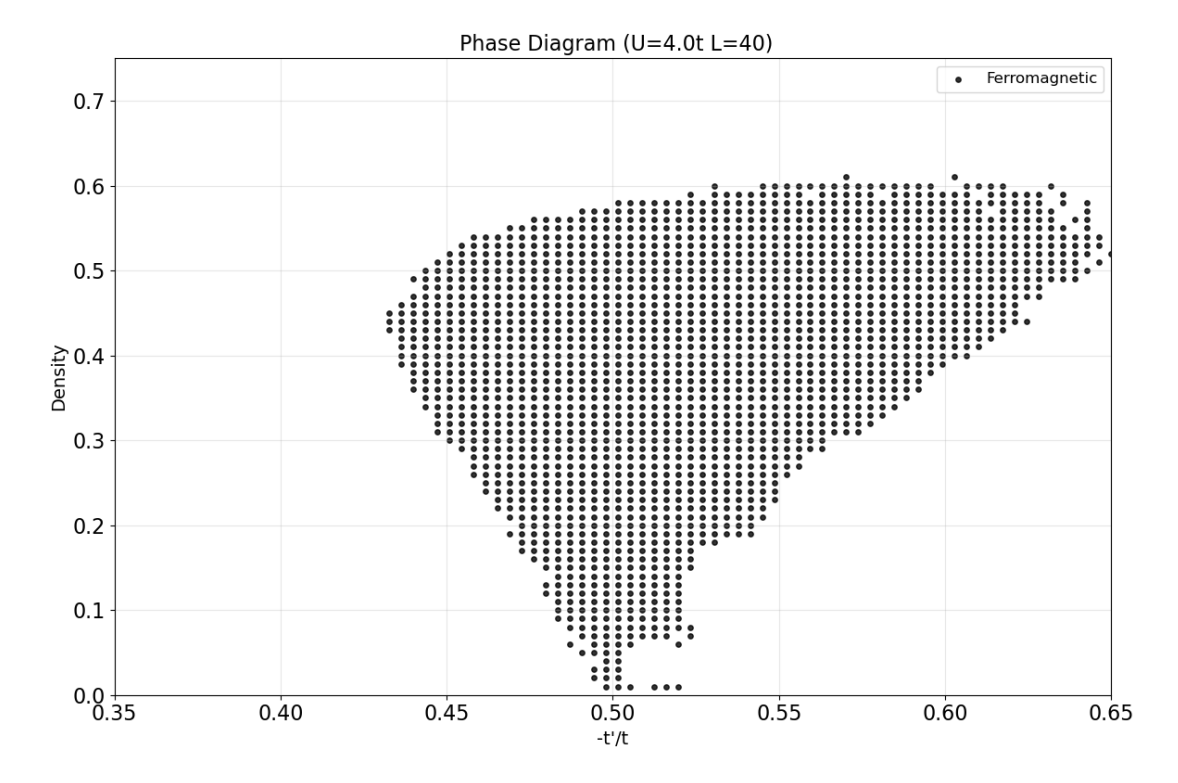


**Figure 4.1.** Two-diagonal hopping case: phase diagram for lattice size L=40 and interaction strength U=4t.

Figure 4.1 and 4.2 display the ferromagnetic phase diagrams for interaction strengths U=4t and U=8t, respectively. In these plots, the horizontal axis represents the hopping ratio t'/t. The vertical axis indicates the electron filling density n.

Figure 4.1 shows the ferromagnetic phase diagram at moderate interaction strength U = 4t. The ferromagnetic region is relatively limited: it appears only at densities  $n \leq 0.6$ , and requires t'/t values large than 0.43.

Figure 4.2 reveals a dramatically expanded ferromagnetic region covering densities  $n \lesssim 0.95$  and extending down to moderate frustration levels  $(t'/t \gtrsim 0.3)$ . The interaction energy now dominates over kinetic costs, stabilizing ferromagnetism across most of the parameter space.

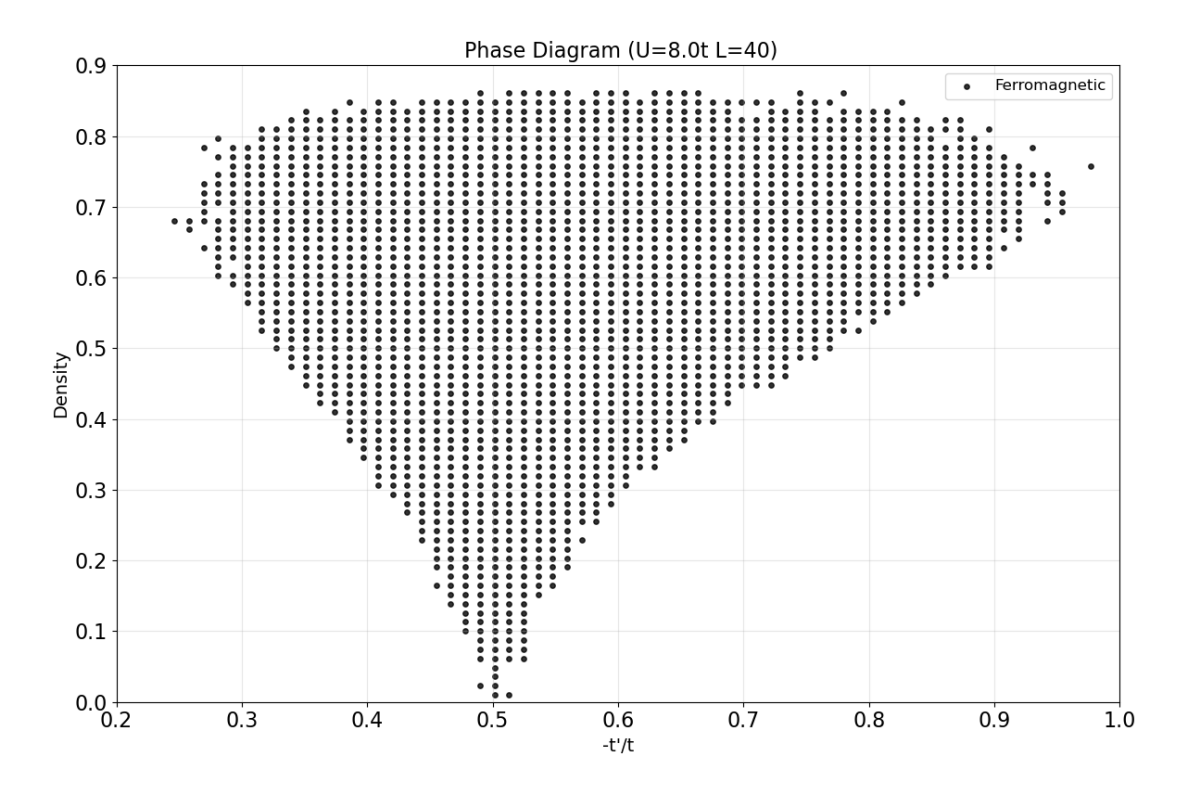


**Figure 4.2.** Two-diagonal hopping case: phase diagram for lattice size L=40 and interaction strength U=8t.

In Hlubina's paper [67], they do the same calculation and get the results as shown in Fig 4.3 and 4.4. The fluctuations in my phase diagrams are probably due to finite-size effects. The fact that Hlubina's phase diagram is more regular is probably due to the use of an interpolating curve when constructing the diagram.

Importantly, at low densities our findings, as well as those of Hlubina, are consistent with the boundary reported in the paper published by Pieri in 1996 [28], which established that, in the limit  $n \to 0$ , a fully polarized ferromagnetic ground state can occur only for -0.20 > t'/t > -0.65.

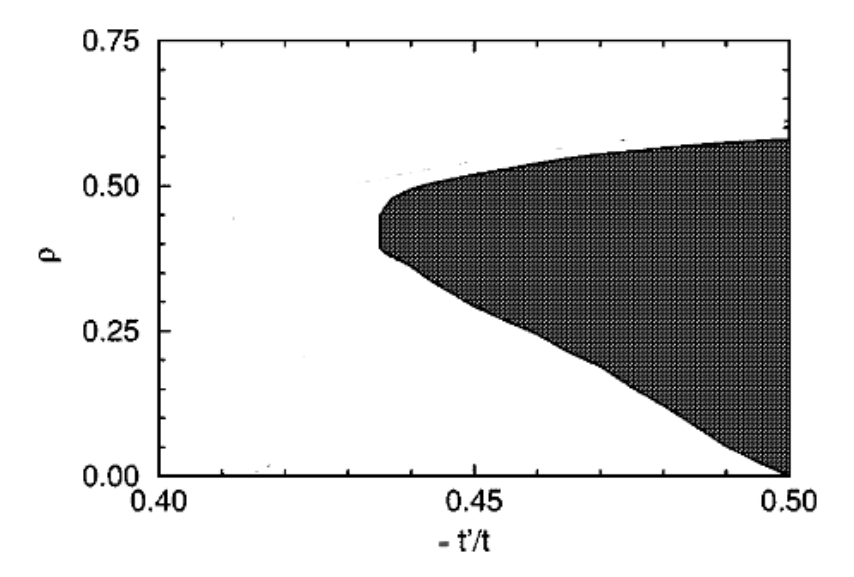


**Figure 4.3.** Two-diagonal hopping case: phase diagram for lattice size L=32 and interaction strength U=4t in Hlubina 's paper.

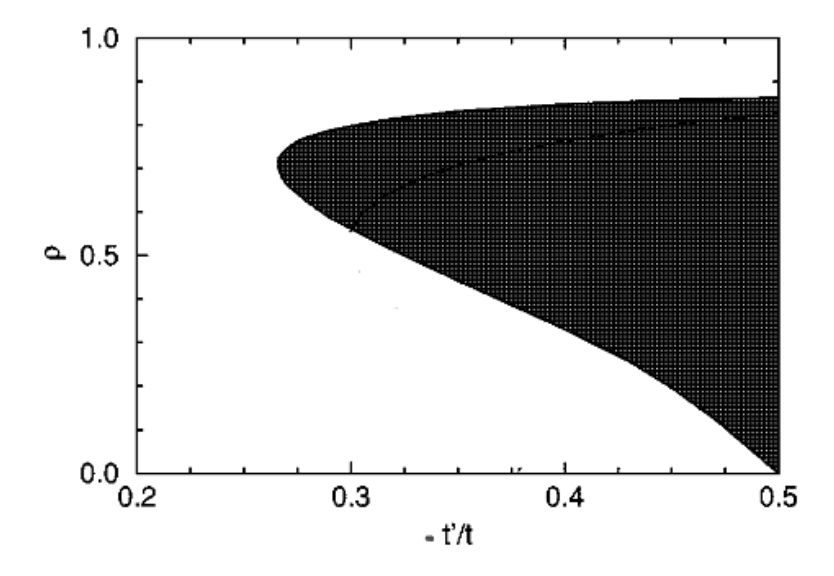


**Figure 4.4.** Two-diagonal hopping case: phase diagram for lattice size L=32 and interaction strength U=8t in Hlubina's paper.

The comparison between these two cases illustrates the cooperative effect of interaction strength and lattice geometry. When U=4t, the kinetic energy cost of spin polarization is comparable to the interaction-driven energy gain, making

ferromagnetism fragile and dependent on both moderate density and strong frustration. However, when U = 8t, the interaction energy dominates, suppressing double occupancy and favoring spin-polarized configurations even without large values of t'.

This behavior aligns with the theoretical understanding that large U enhances ferromagnetic stability by penalizing double occupancy, while lattice frustration weakens antiferromagnetic correlations that would otherwise compete with ferromagnetic order.

### 4.1.2 One-Diagonal Hopping Case

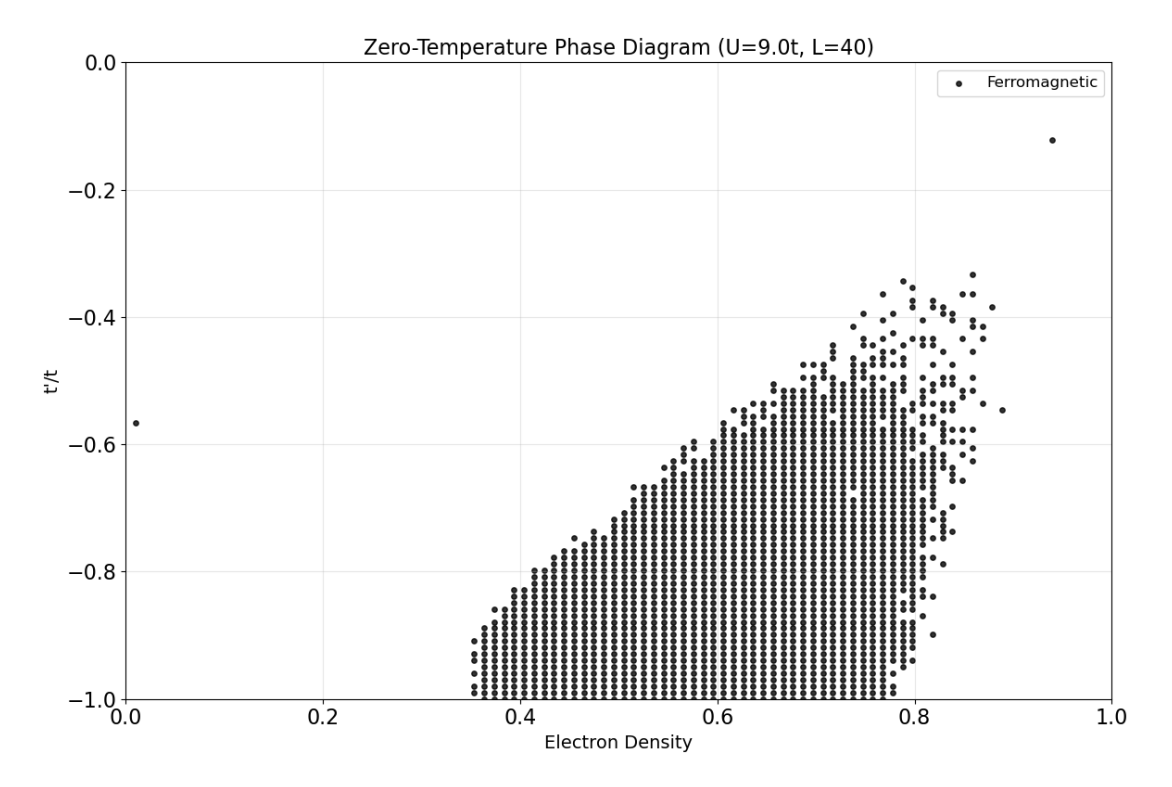


**Figure 4.5.** One-diagonal hopping case: phase diagram for lattice size L=40 and interaction strength U=9t.

Next, we investigate the model with the one-diagonal hopping dispersion described in Eq.2.44. We also perform calculations on a finite lattice with size L=40. The resulting phase diagrams are shown in Figure 4.5 and 4.6 for interaction strengths

U = 9t and U = 13t, respectively. Note that in this case, the vertical axis represents t'/t while the horizontal axis shows the filling density n.

Figure 4.5 reveals a qualitatively different phase structure compared to the two-diagonal case. The ferromagnetic region exhibits a wedge-shaped distribution, primarily located at negative values of t'/t (corresponding to configurations away from the square lattice limit). An important observation is the density-dependent behavior: higher densities require less severe lattice frustration to stabilize ferromagnetism, while lower densities demand stronger frustration.

A particularly notable feature is the emergence of a small ferromagnetic region near  $t' \approx -0.5t$  in the low-density limit ( $n \to 0$ ). This ferromagnetic phase is attributed to the Müller-Hartmann mechanism[37], which we have already discussed in section 1.3.

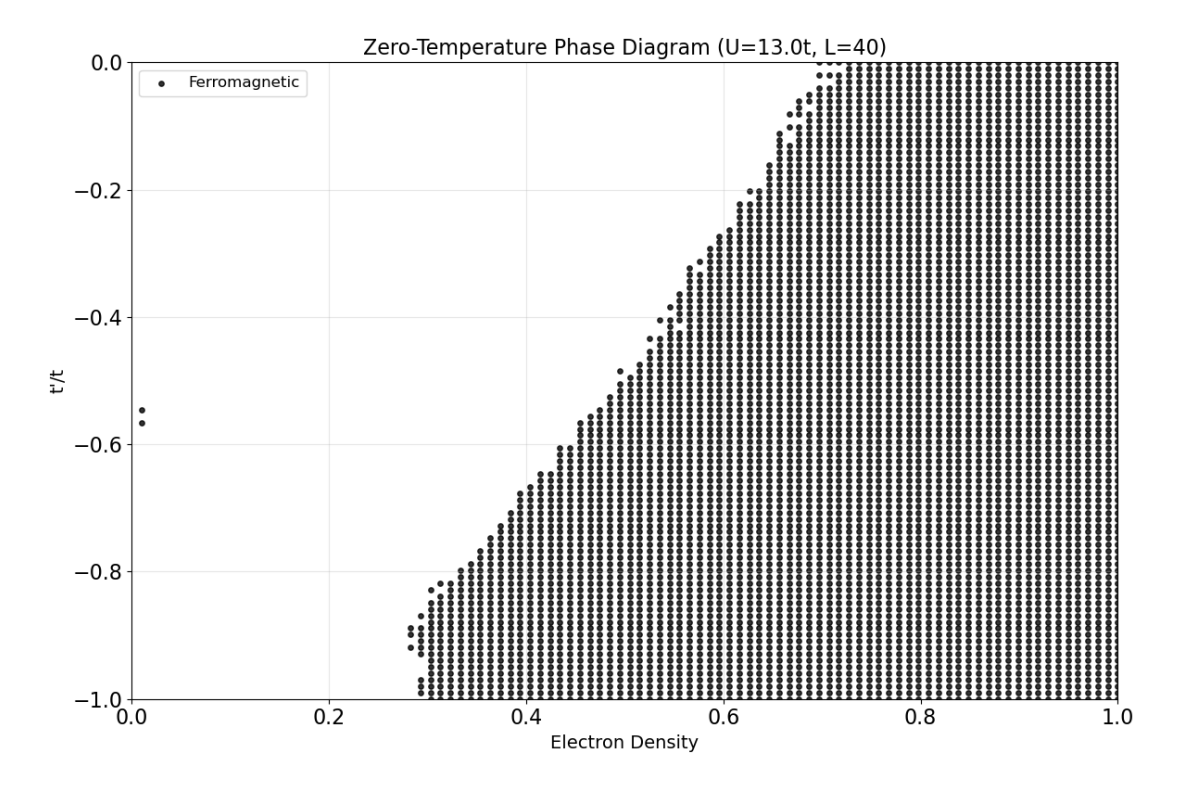


**Figure 4.6.** One-diagonal hopping case: phase diagram for lattice size L=40 and interaction strength U=13t.

When U increases to 13t in Figure 4.6, the ferromagnetic region expands significantly toward lower densities and less restrictive frustration requirements. The

phase boundary becomes more regular and continuous, extending toward the lowerleft region of the parameter space.

Near half-filling (  $n \approx 1$  ), the results are consistent with Nagaoka ferromagnetism, which is theoretically established for single-hole doping in the infinite-U limit. Our numerical results demonstrate that Nagaoka-type ferromagnetism persists even at finite U=13t within the density range 0.8 < n < 1, consistent with previous numerical studies. In this regime, the critical  $t_c'$  decreases as density reduces from half-filling, exhibiting opposite behavior compared to the low-density regime.

Comparing the one-diagonal and two-diagonal cases reveals that the specific form of the dispersion relation significantly influences both the density threshold for ferromagnetism and the geometrical dependence on t'/t. This demonstrates that band structure details, beyond simple frustration considerations, play a crucial role in determining ferromagnetic stability.

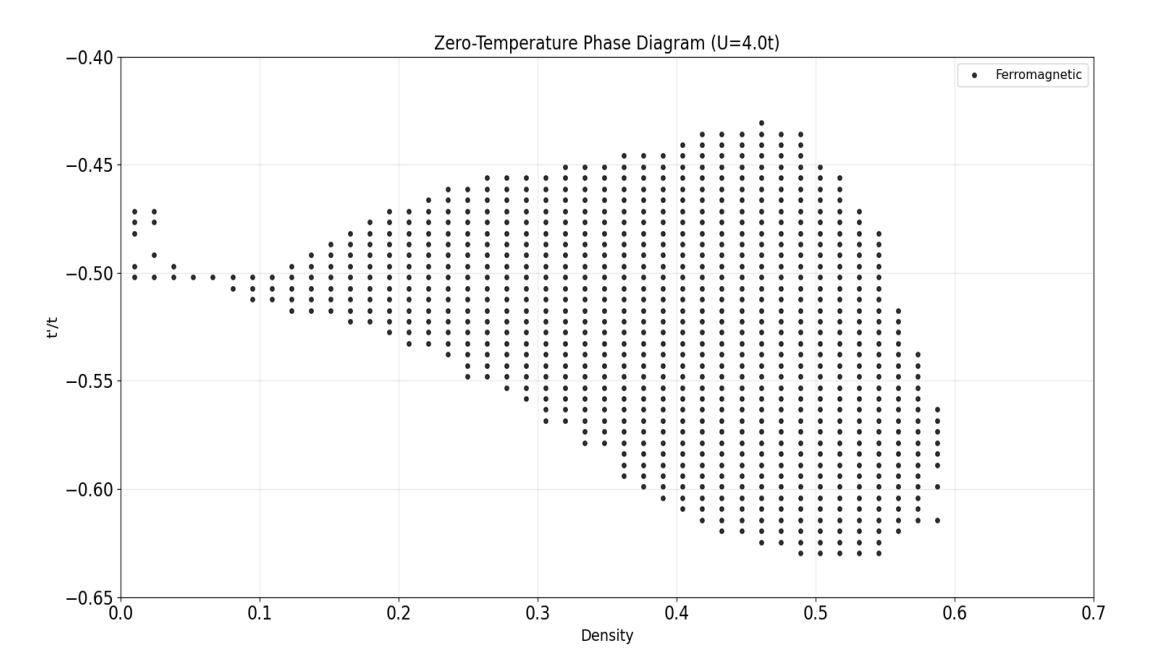
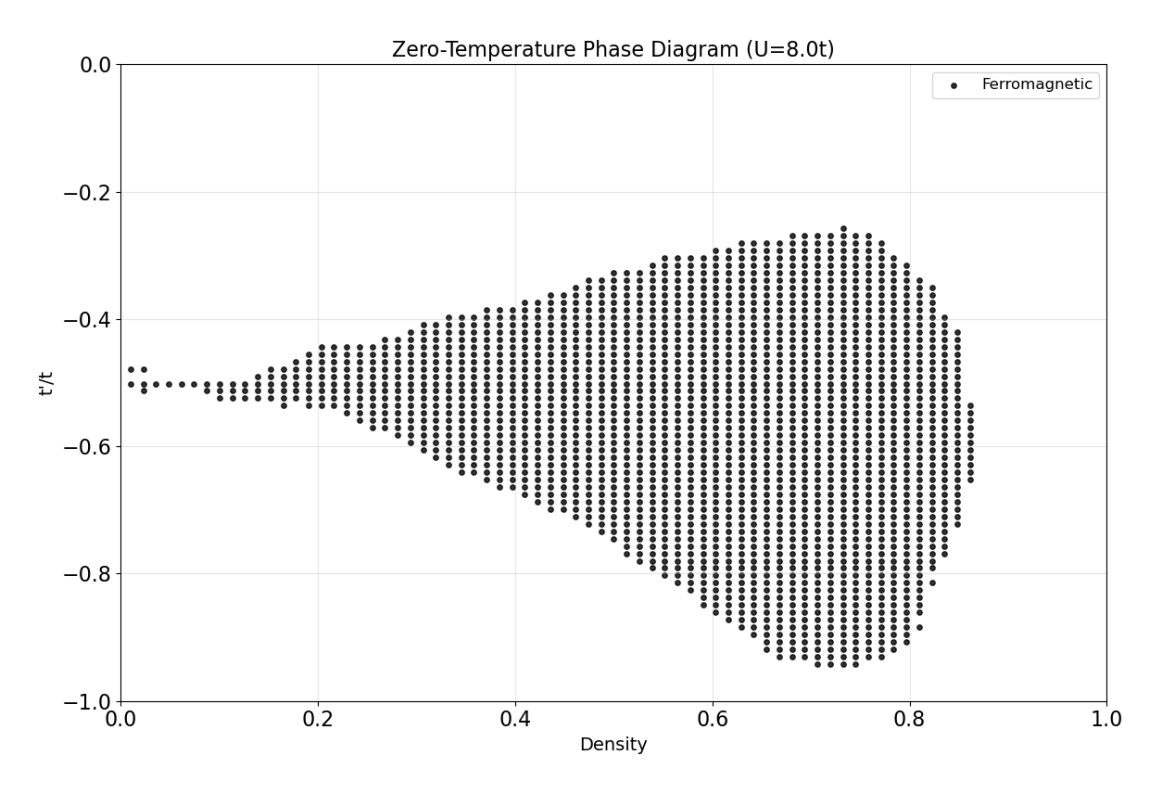


**Figure 4.7.** Two-diagonal hopping case: phase diagram in the thermodynamic limit for interaction strength U = 4t.

## 4.2 Thermodynamic Limit Analysis

To validate our finite-lattice results and obtain more accurate phase boundaries, we extend the calculations to the thermodynamic limit by replacing discrete momentum summations with continuous integrals over the first Brillouin zone.

### 4.2.1 Two-Diagonal Hopping Case



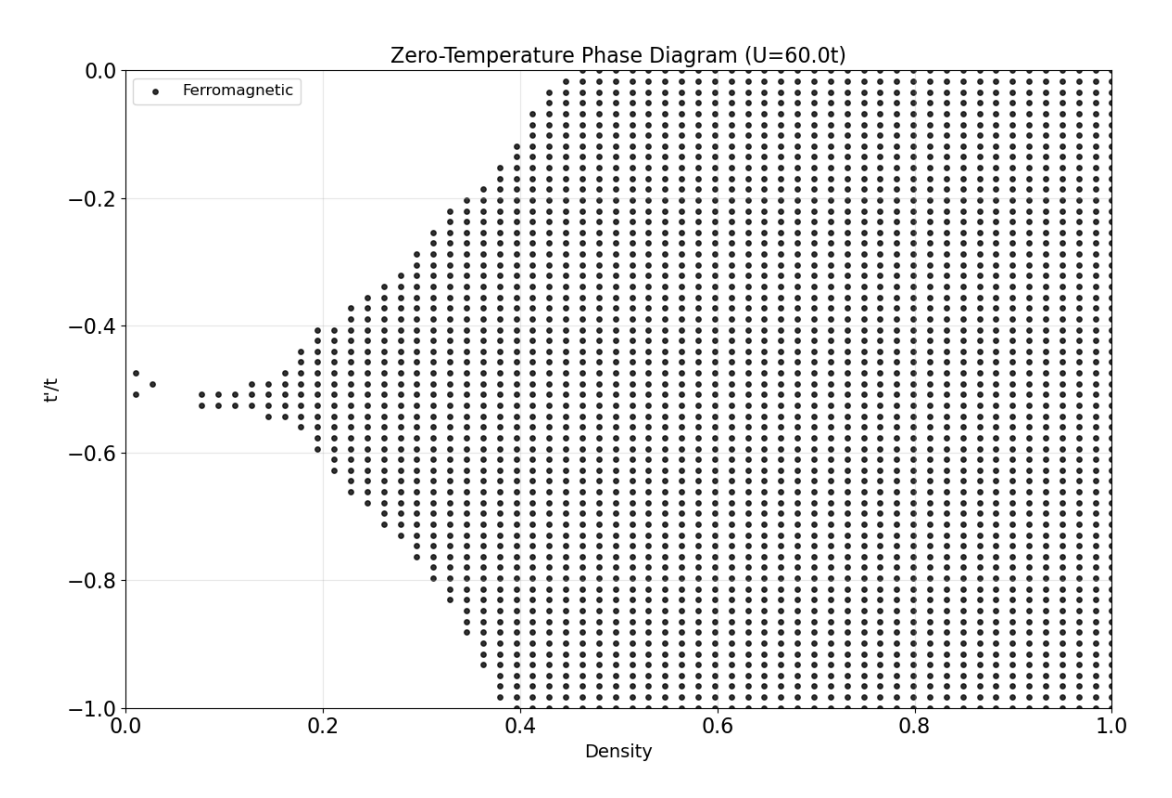
**Figure 4.8.** Two-diagonal hopping case: phase diagram in the thermodynamic limit for interaction strength U = 8t.

Figure 4.7 and 4.8 present the ferromagnetic phase diagrams in the thermodynamic limit for U = 4t and U = 8t, respectively.

Comparing Figure 4.7 with 4.1 and 4.8 with 4.2 we can observe that systems with the same U parameter exhibit a consistent density range within the ferromagnetic region. However, the discrete system displays a rough, irregular boundary, which is indicative of finite-size effects and statistical fluctuations arising from its

limited system size. In contrast, the thermodynamic limit presents a smoother, more regular ferromagnetic region, reflecting the continuous behavior of an infinite system where such fluctuations are effectively averaged out. These findings underscore the influence of finite-size effects on the ferromagnetic phase across different scenarios.

Figure 4.9 4.10 show the phase diagram for U=60t and U=200t, we can find that the ferromagnetism change very little so U=200t can be considered representative of the  $U=+\infty$  limit. The figure indicates that under a strong interaction potential, the interaction between particles in the system is enhanced, and particles are more inclined to form ordered ferromagnetic arrangements. Thus, the system is more likely to form a ferromagnetic ordered state within a wider range of density and energy parameter intervals.



**Figure 4.9.** Two-diagonal hopping case: phase diagram in the thermodynamic limit for interaction strength U = 60t.

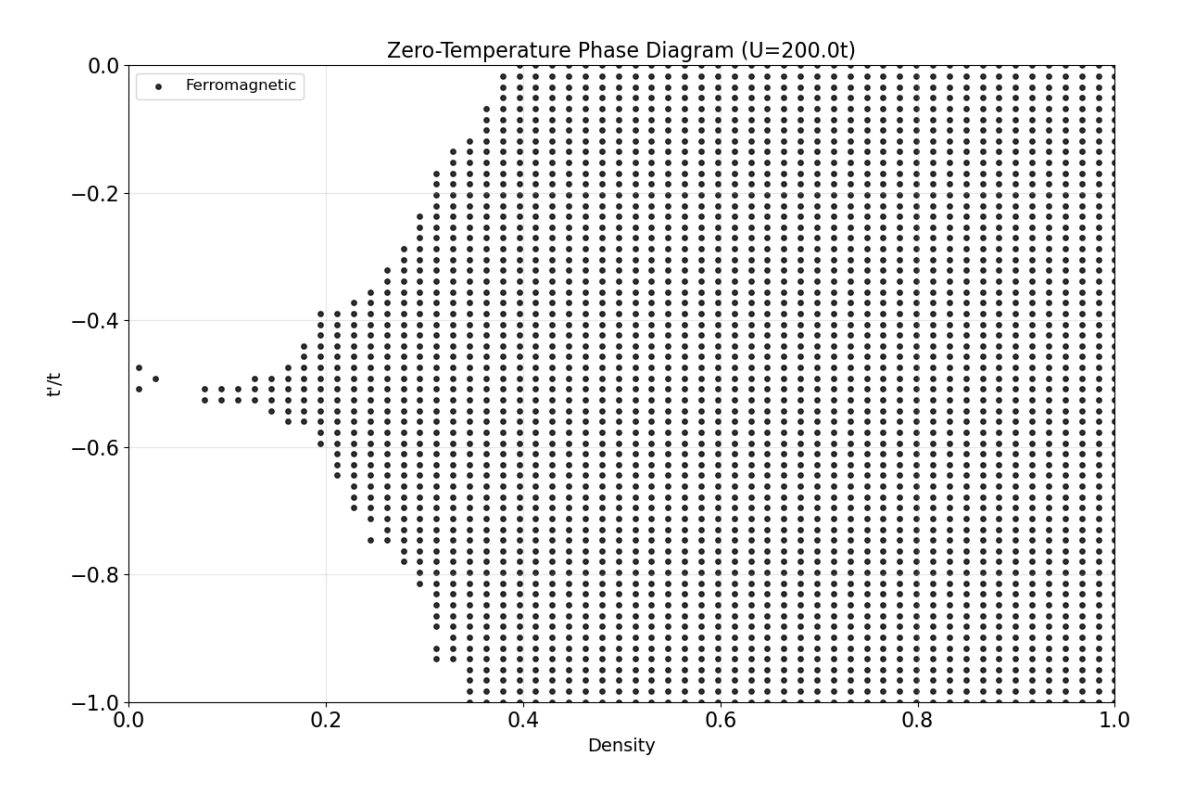


**Figure 4.10.** Two-diagonal hopping case: phase diagram in the thermodynamic limit for interaction strength U = 200t, approximating the  $U = +\infty$  limit.

### 4.2.2 One-Diagonal Hopping case

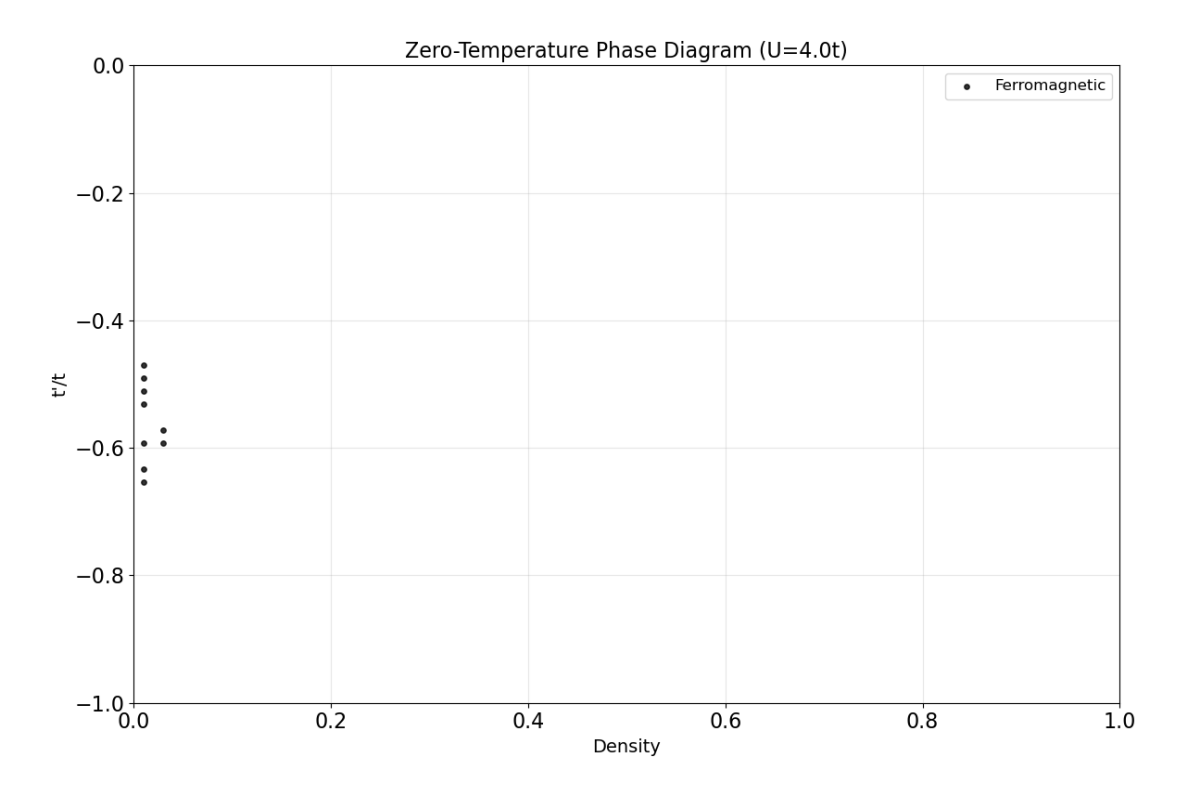


**Figure 4.11.** One-diagonal hopping case: phase diagram in the thermodynamic limit for interaction strength U = 4t.

Figure 4.11 through 4.17 show the evolution of the ferromagnetic phase diagram in the thermodynamic limit as the interaction strength increases from U = 4t to U = 17t.

By comparing the phase diagrams for the one-hopping case as shown in Figures 4.114.12 and the two-hopping case as shown in Figures 4.7 4.8, we can observe distinct differences in the ferromagnetic phases induced by different band dispersion under the same interaction strength. For example, for the one-hopping case (U=4t), ferromagnetism only emerges in the density  $(n \to 0)$  and only near a specific value of the hopping ratio (t'/t), this type of ferromagnetism is known as the Müller-Hartmann ferromagnetism. In contrast, for the two-hopping case (U=4t), a continuous ferromagnetic region is formed, spanning a relatively broad range of both electron densities and t'/t values. From these observations, we conclude that

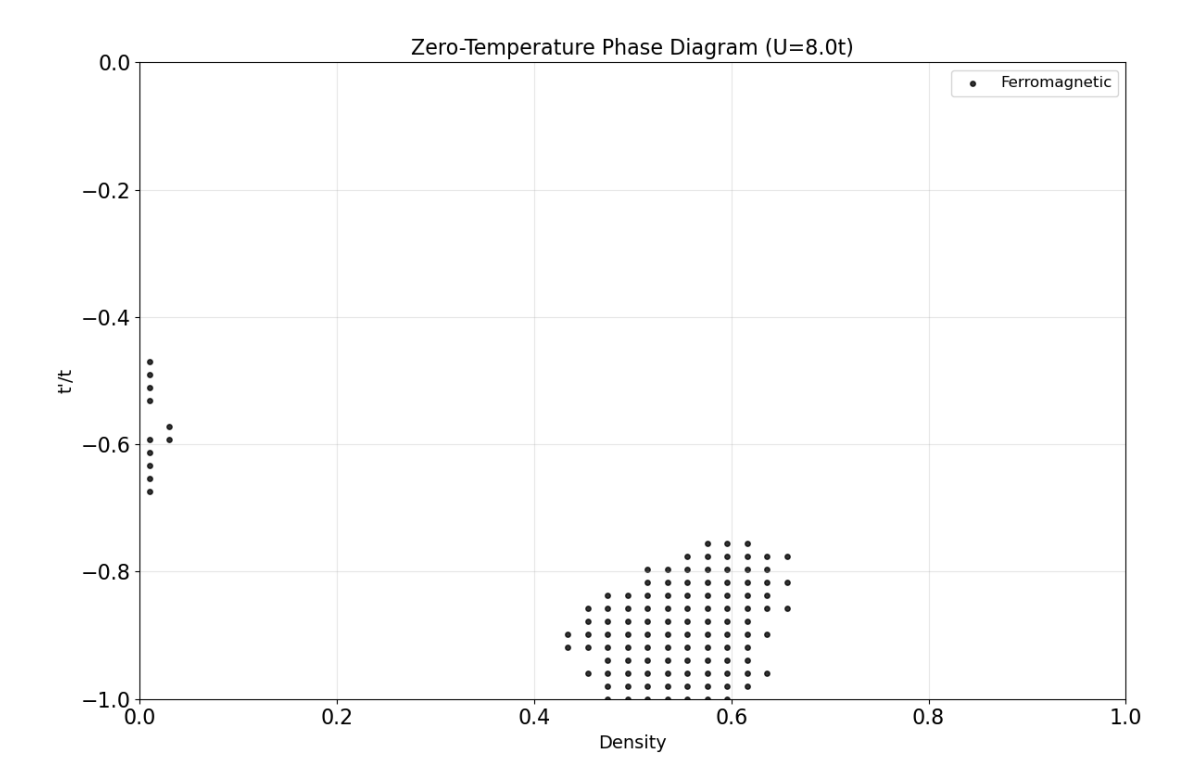


**Figure 4.12.** One-diagonal hopping case: phase diagram in the thermodynamic limit for interaction strength U = 8t.

band dispersion exerts a significant influence on the stability of ferromagnetism.

By comparing the discrete system in U=9t as shown in Figures 4.5 and the thermodynamics limit system as shown in Figures 4.13, we can observe that both systems exhibit a consistent density range within the ferromagnetic region. As we discussed previously, the discrete system has a rough boundary due to the finite - size effects. Moreover, in both systems, we can observe the Müller - Hartmann ferromagnetism.

As U increases from 9t to 17t, the ferromagnetic region expands systematically, covering progressively wider density intervals and becoming stable under less restrictive frustration conditions. This trend confirms that stronger on-site repulsion enhances ferromagnetic stability by suppressing charge fluctuations and favoring spin-polarized configurations.

Figure 4.18 4.19 show the phase diagram for U = 60t and U = 200t, we can find that the ferromagnetism change very little so U = 200t can be considered

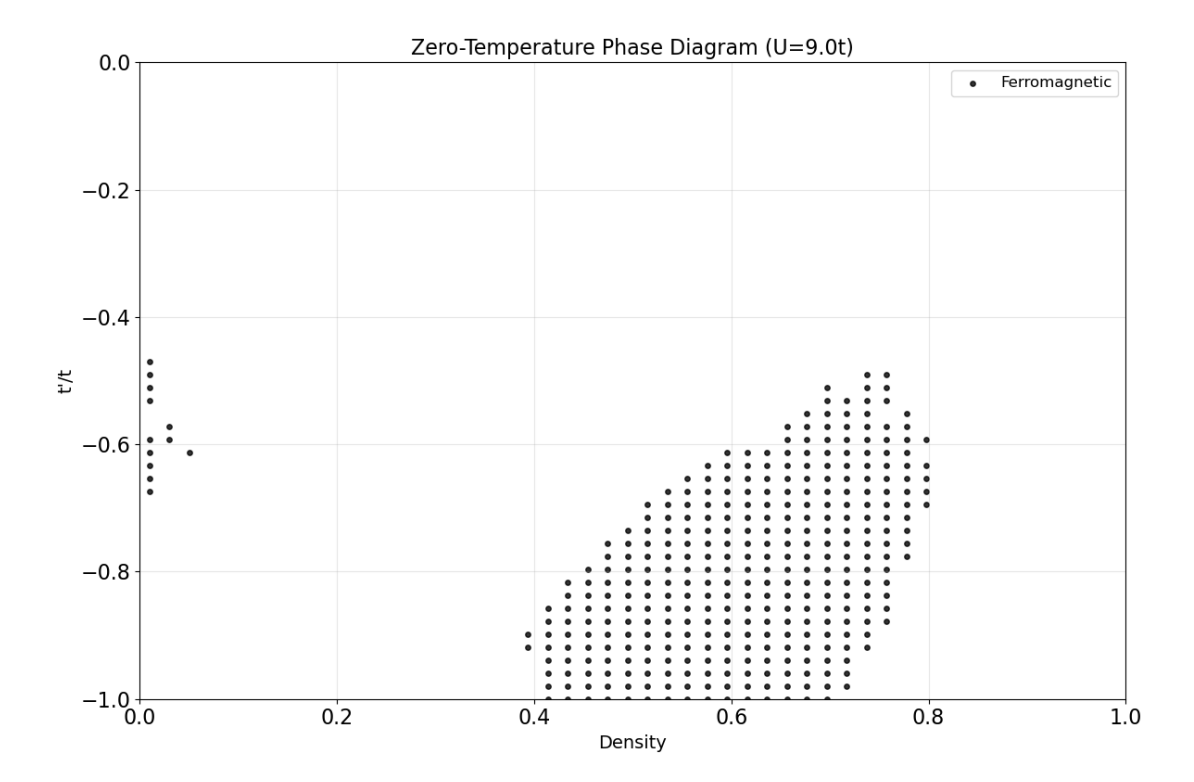


**Figure 4.13.** One-diagonal hopping case: phase diagram in the thermodynamic limit for interaction strength U = 9t.

representative of the  $U=+\infty$  limit. The broad ferromagnetic region reflects the effectiveness of both Nagaoka ferromagnetism (near half-filling) and Müller-Hartmann ferromagnetism (at low densities) when double occupancy is strongly suppressed.

To summarize, we find interaction strength plays a critical role in stabilizing ferromagnetism: weak interactions ( $U \le 4t$ ) in density n = 0.4 require large geometrical frustration to sustain ferromagnetic order, while strong interactions ( $U \ge 8t$ ) enable ferromagnetism across broad parameter ranges with a smaller degree of frustration. Second, the phase structure exhibits distinct dispersion dependence: two-diagonal hopping favors ferromagnetism near t'/t = -0.5, where the band dispersion develops two degenerate minima, whereas one-diagonal hopping supports multiple ferromagnetic mechanisms across different density regimes. Third, lattice size effects ferromagnetism.

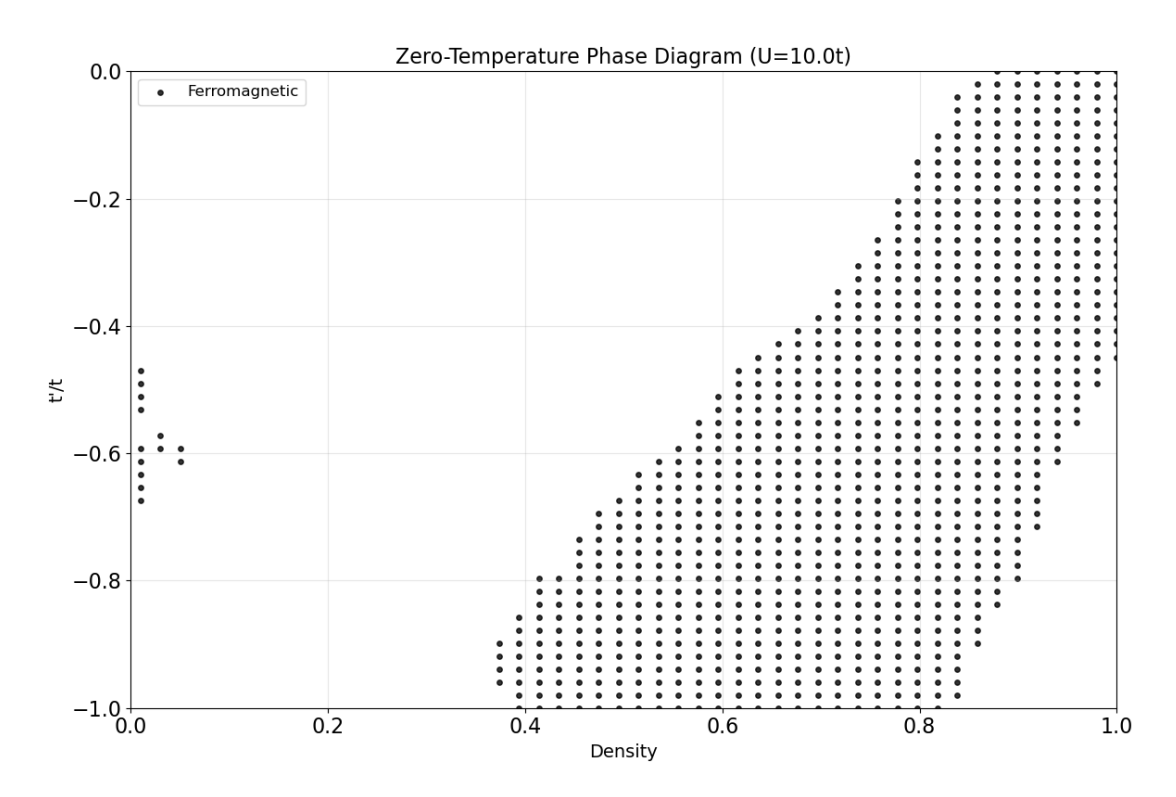


**Figure 4.14.** One-diagonal hopping case: phase diagram in the thermodynamic limit for interaction strength U = 10t.

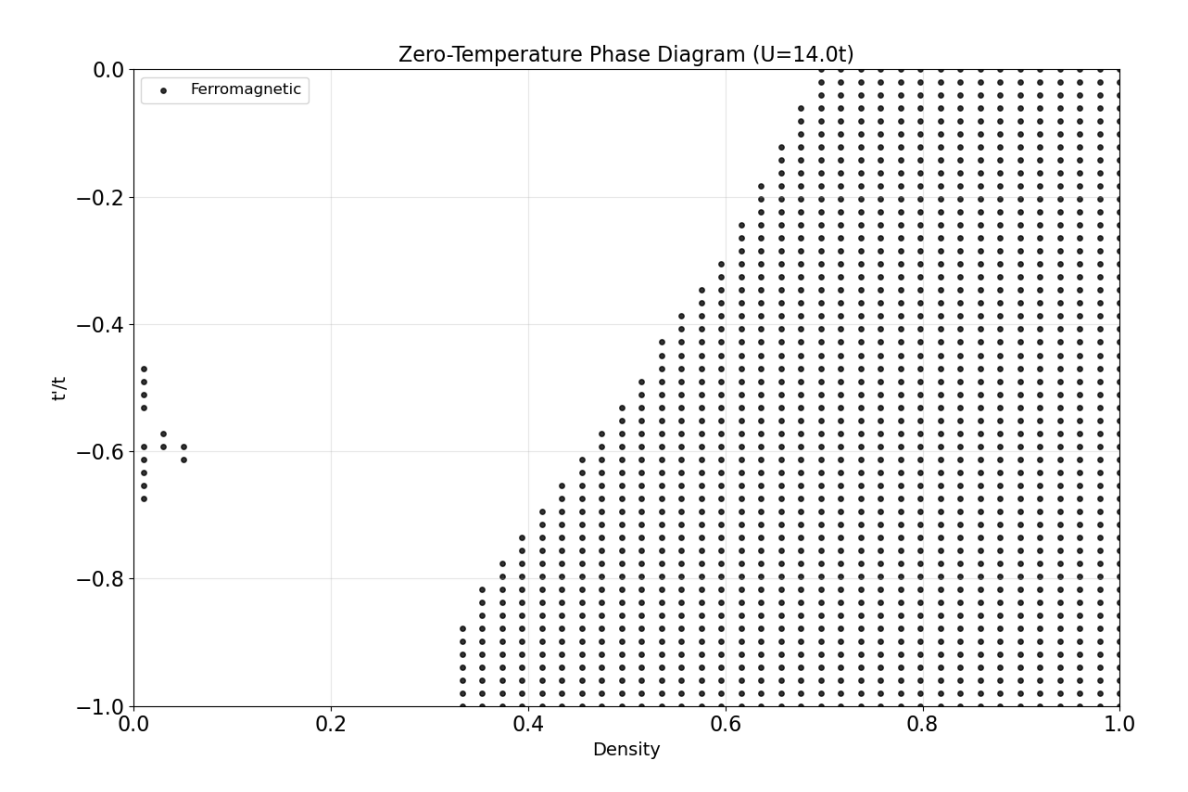


**Figure 4.15.** One-diagonal hopping case: phase diagram in the thermodynamic limit for interaction strength U = 14t.

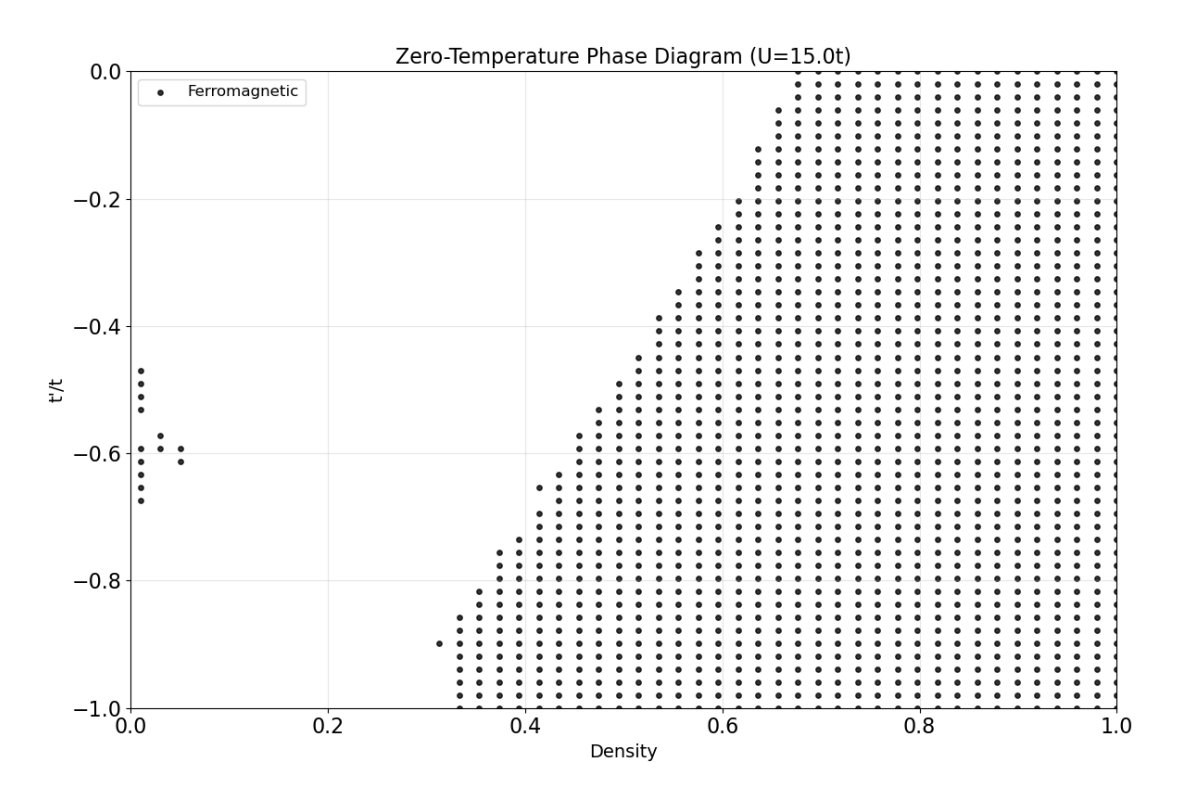


**Figure 4.16.** One-diagonal hopping case: phase diagram in the thermodynamic limit for interaction strength U=15t.

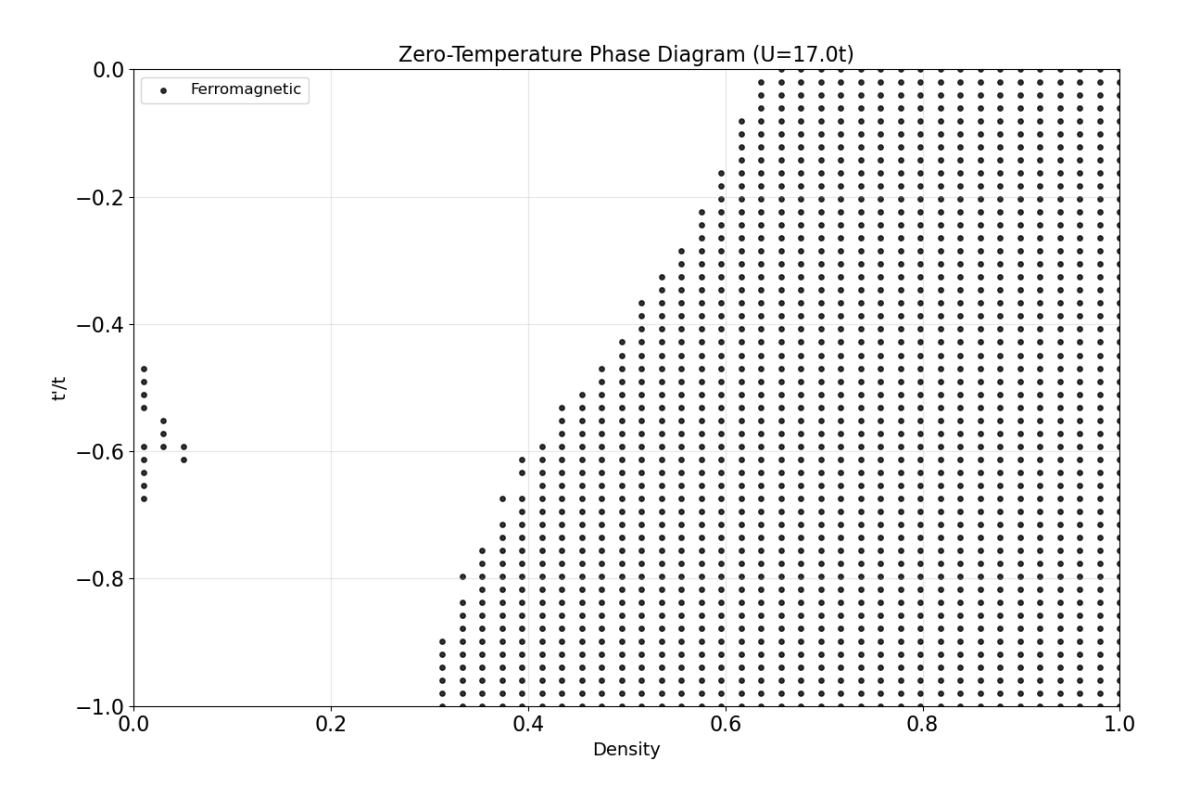


**Figure 4.17.** One-diagonal hopping case: phase diagram in the thermodynamic limit for interaction strength U = 17t.

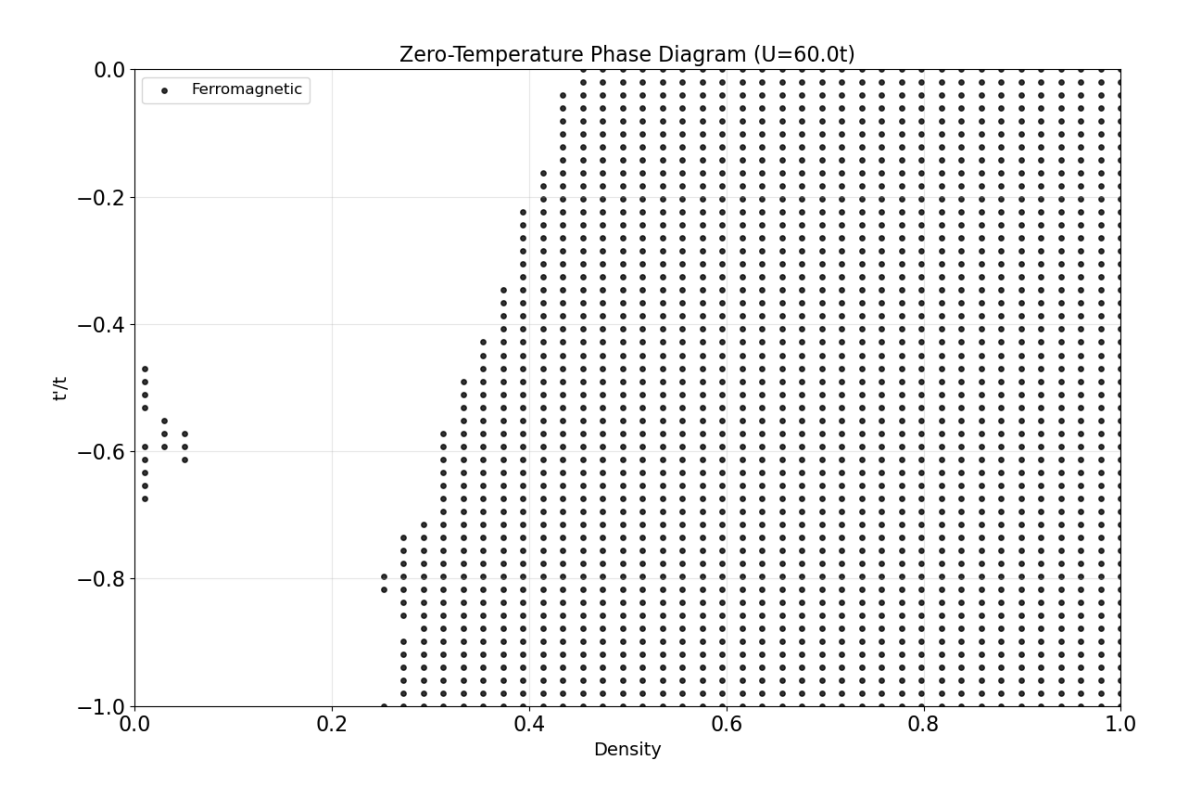


**Figure 4.18.** One-diagonal hopping case: phase diagram in the thermodynamic limit for U = 60t.

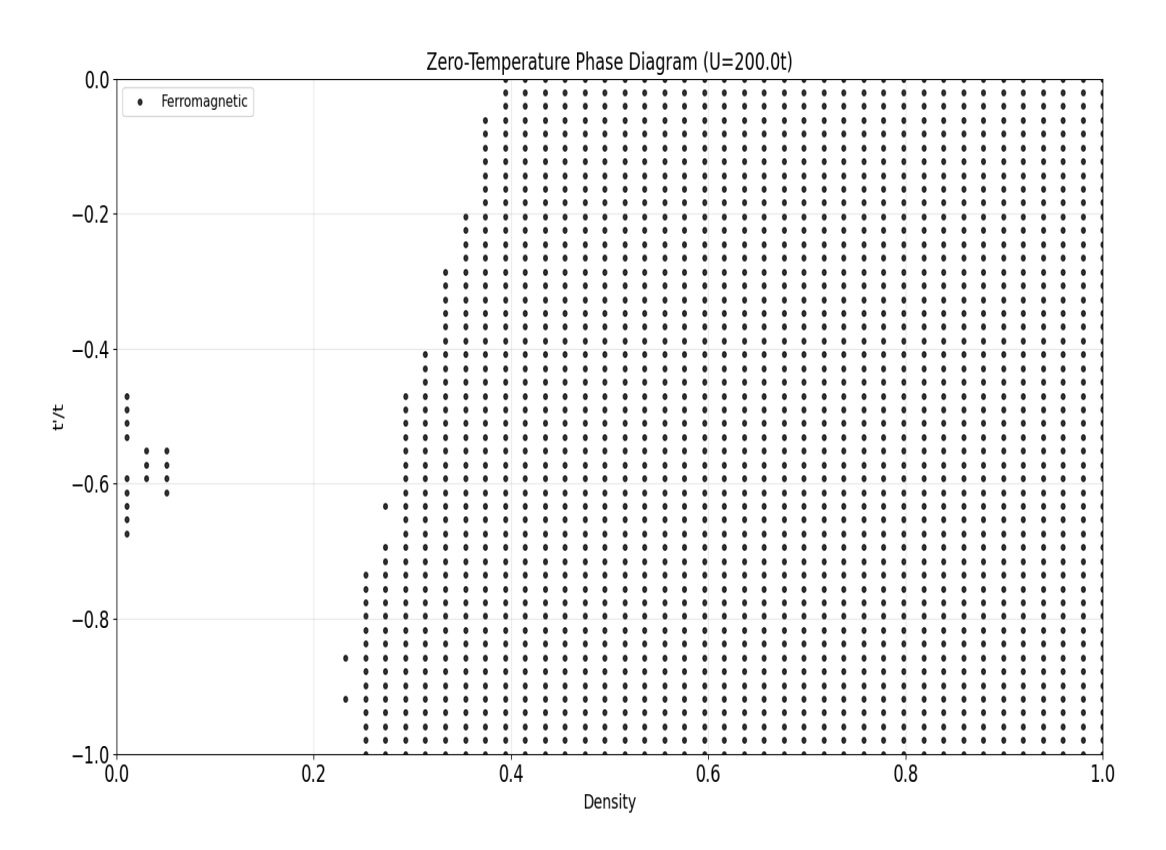


**Figure 4.19.** One-diagonal hopping case: phase diagram in the thermodynamic limit for U=200t, approximating the  $U=+\infty$  limit.

## Chapter 5

## Conclusions and Outlooks

#### 5.1 Conclusions

This thesis provides a numerical investigation of ferromagnetism in the Hubbard model, revealing the complex interplay between interaction strength, lattice geometry, and electron density in determining magnetic phase boundaries. Our systematic study of two distinct lattice dispersions demonstrates that ferromagnetic order emerges through fundamentally different mechanisms depending on the parameter regime.

The role of interaction strength proves to be paramount in stabilizing ferromagnetic phases. At moderate interactions (U=4t to U=9t), ferromagnetism appears only in restricted regions of the phase diagram, requiring specific combinations of electron density and lattice frustration. However, as the interaction strength increases beyond  $U \gtrsim 8t$ , the ferromagnetic region expands dramatically, eventually dominating most of the phase diagram in the strong-coupling limit (U=200t). This behavior reflects the fundamental physics of the Hubbard model, where strong on-site repulsion suppresses double occupancy and favors spin-polarized configurations that minimize interaction energy at the expense of kinetic energy.

Lattice geometry, controlled through the hopping ratio t'/t, provides a crucial tuning parameter for ferromagnetic stability. The interpolation between square lattice (t'=0) and triangular lattice limits in the one-diagonal hopping case reveals

that geometrical frustration suppresses antiferromagnetic correlations, thereby creating favorable conditions for ferromagnetic order. Notably, the two dispersion types exhibit qualitatively different dependencies on lattice geometry, with the one-diagonal hopping case showing ferromagnetism in extended regions of the phase diagram, while the two-diagonal hopping case favors ferromagnetism close to t'/t = -0.5, where the band develops tow degenerate minima.

The comparison between finite-lattice and thermodynamic-limit calculations reveals important finite-size effects that must be considered when interpreting numerical results. In particular, our results for the one-diagonal hopping case shows quite a good agreement with the finding of the experimental work [4] for both system size.

Our analysis identifies distinct physical mechanisms underlying ferromagnetism in different parameter regimes. Near half-filling, the observed ferromagnetism can be attributed to the Nagaoka mechanism, where hole doping into a strongly interacting system leads to spin polarization. In contrast, at low electron densities, we observe signatures of the Müller-Hartmann mechanism, where ferromagnetism emerges due to the specific interplay between band structure and correlation effects. The coexistence and competition between these mechanisms creates a rich phase diagram with multiple ferromagnetic regions separated by paramagnetic phases.

These results establish the T-matrix approach as a reliable and efficient approach for mapping magnetic phase diagrams in strongly correlated electron systems. The method successfully captures the essential physics of ferromagnetic transitions while remaining computationally tractable for systematic parameter studies. The comprehensive phase diagrams presented here provide valuable benchmarks for future theoretical and experimental investigations of frustrated magnetic systems, and demonstrate the rich physics that emerges from the seemingly simple Hubbard model when lattice geometry and strong correlations are considered together.

#### 5.2 Outlooks

The present work opens several promising avenues for future research that could significantly deepen our understanding of ferromagnetism in frustrated lattice systems. While our T-matrix approach has proven effective for identifying ferromagnetic phase boundaries, extending this approach to include dynamical properties would provide crucial insights into the nature of magnetic excitations and finite-temperature behavior. Incorporating spin wave calculations and examining the stability of ferromagnetic states against thermal fluctuations represents a natural next step that would bridge the gap between our zero-temperature ground state analysis and experimentally accessible temperature regimes.

The exploration of more complex lattice geometries presents another fertile direction for future investigations. Our current study focused on interpolations between square and triangular lattices, but real materials often exhibit more intricate structural features such as kagome lattices, honeycomb structures, or three-dimensional frustrated networks. Extending the present approach to these geometries could reveal new classes of ferromagnetic phases and provide theoretical guidance for material design. Particularly intriguing is the possibility of engineering artificial lattices through cold atom systems or photonic crystals, where the hopping parameters and interaction strengths can be tuned independently to explore parameter regimes inaccessible in conventional solid-state systems.

The inclusion of longer-range interactions represents a crucial extension that would enhance the relevance of our model to real materials. While the on-site Hubbard interaction provides the essential physics of strong correlations, many transition metal compounds exhibit significant nearest-neighbor and even longer-range Coulomb interactions. Incorporating these additional interaction terms could fundamentally alter the phase diagram and potentially stabilize novel magnetic phases not captured by the purely on-site model. Moreover, the interplay between geometric frustration and extended interactions may give rise to exotic quantum phases such as spin liquids or unconventional superconducting states.

From an experimental perspective, our theoretical predictions provide clear targets for verification in quantum simulator platforms. Cold atomic gases in optical lattices offer unprecedented control over lattice geometry and interaction strength,

making them ideal systems for testing our phase diagrams quantitatively. Recent advances in quantum gas microscopy enable direct observation of magnetic correlations with single-site resolution, potentially allowing for detailed comparison with our theoretical results. Similarly, the rapidly developing field of moiré materials in twisted van der Waals heterostructures provides natural realizations of frustrated lattices with tunable parameters, offering another promising platform for experimental validation.

Finally, the rich phase diagrams uncovered in this study motivate deeper investigations into the quantum critical points separating different magnetic phases. Understanding the universality classes of these transitions and their associated critical exponents would provide fundamental insights into the nature of quantum phase transitions in frustrated systems. Such knowledge could have far-reaching implications for understanding quantum magnetism in real materials and potentially guide the discovery of new quantum phases of matter with exotic properties relevant for future technological applications.

## Appendix I

# Monte Carlo Integration

## Background

Monte Carlo integration is a numerical integration technique based on random sampling, particularly useful for evaluating integrals in high-dimensional or complex domains. Its core idea leverages the Law of Large Numbers, approximating the expected value of an integral by the average of random samples. The method was developed in the 1940s by scientists such as Stanislaw Ulam and John von Neumann, and its name pays homage to the Monte Carlo Casino in Monaco, reflecting the inherent randomness of the technique.

### **Mathematical Foundation**

Consider the integral of a function  $f(\mathbf{x})$  over a domain  $\Omega \subset \mathbb{R}^d$ :

$$I = \int_{\Omega} f(\mathbf{x}) d\mathbf{x}.$$

If there exists a probability density function (PDF)  $p(\mathbf{x})$  defined on  $\Omega$  such that  $p(\mathbf{x}) > 0$  and  $\int_{\Omega} p(\mathbf{x}) d\mathbf{x} = 1$ , the integral can be expressed as an expectation:

$$I = \int_{\Omega} \frac{f(\mathbf{x})}{p(\mathbf{x})} p(\mathbf{x}) d\mathbf{x} = \mathbb{E} \left[ \frac{f(\mathbf{X})}{p(\mathbf{X})} \right],$$

where **X** is a random variable distributed according to  $p(\mathbf{x})$ . By the Law of Large Numbers, drawing N independent and identically distributed (i.i.d.) samples  $\{\mathbf{x}_1, \mathbf{x}_2, \dots, \mathbf{x}_N\}$  from  $p(\mathbf{x})$ , the sample mean,

$$\hat{I}_N = \frac{1}{N} \sum_{i=1}^N \frac{f(\mathbf{x}_i)}{p(\mathbf{x}_i)},$$

converges almost surely to I as  $N \to \infty$ .

## Algorithmic Procedure

The standard Monte Carlo integration procedure consists of the following steps:

- 1. Select a probability density function (PDF)  $p(\mathbf{x})$ : A common choice for bounded domains  $\Omega$  is the uniform distribution, i.e.,  $p(\mathbf{x}) = 1/|\Omega|$ , where  $|\Omega|$  denotes the volume of the domain.
- 2. Generate random samples: Draw N independent samples  $\{\mathbf{x}_1, \mathbf{x}_2, \dots, \mathbf{x}_N\}$  from the distribution  $p(\mathbf{x})$ .
- 3. Compute function values: For each sample, compute the value  $f(\mathbf{x}_i)/p(\mathbf{x}_i)$ .
- 4. Estimate the integral: Calculate the estimate of the integral:

$$\hat{I}_N = \frac{1}{N} \sum_{i=1}^N \frac{f(\mathbf{x}_i)}{p(\mathbf{x}_i)}.$$

5. **Error analysis**: The error of the Monte Carlo estimate typically scales as  $\mathcal{O}(1/\sqrt{N})$ , independent of the dimensionality of the integral. The standard error can be estimated from the sample variance.

## Example: One-Dimensional Integral

To compute the integral  $I = \int_a^b f(x) dx$ :

• Choose the uniform distribution  $p(x) = \frac{1}{b-a}$ .

• The estimator then becomes:

$$\hat{I}_N = \frac{b-a}{N} \sum_{i=1}^N f(x_i).$$

• Generate N uniform random numbers  $x_i$  in [a, b], compute  $f(x_i)$  for each, and average them multiplied by (b - a).

## Appendix II

## Brent's Method for Root-Finding

### Background

Brent's method is a root-finding algorithm for solving nonlinear equations of the form f(x) = 0. Developed by Richard P. Brent in 1971, the method combines the robustness of the bisection method with the speed of interpolation-based methods such as the secant method and inverse quadratic interpolation. It is widely used because it guarantees convergence when the initial interval brackets a root, while often achieving superlinear convergence in practice.

#### Mathematical Foundation

Given a continuous function f(x) on [a, b] with f(a)f(b) < 0, Brent's method adaptively selects one of three steps:

- **Bisection**: Halves the interval, ensuring the root remains bracketed.
- Secant method: Uses linear interpolation between two recent points.
- Inverse quadratic interpolation: Uses three points to approximate the root more accurately.

The method dynamically chooses the most suitable step at each iteration, falling back on bisection if necessary.

### Algorithmic Procedure

A simplified version of the algorithm proceeds as follows:

- 1. Start with [a, b] such that f(a)f(b) < 0.
- 2. Attempt interpolation (secant or quadratic) to estimate the root.
- 3. If the estimate is invalid or unstable, perform a bisection step.
- 4. Update the bracketing interval.
- 5. Repeat until convergence within a chosen tolerance.

### Error and Convergence

The method is guaranteed to converge linearly in the worst case (as in the bisection method) but usually achieves faster superlinear convergence, combining reliability with efficiency.

### Example

Consider the equation  $f(x) = \cos(x) - x$ . Starting from the interval [0, 1], Brent's method converges rapidly to the solution

$$x \approx 0.739$$
,

illustrating both stability and efficiency.

## **Bibliography**

- [1] H. Tasaki. The hubbard model an introduction and selected rigorous results. J. Phys.: Condens. Matter, 10:4353, 1998.
- [2] H. Tasaki. From nagaoka's ferromagnetism to flat-band ferromagnetism and beyond: An introduction to ferromagnetism in the hubbard model. *Prog.* Theor. Phys., 99:489, 1998.
- [3] M. Qin, T. Schäfer, S. Andergassen, P. Corboz, and E. Gull. The hubbard model: A computational perspective. Annu. Rev. Condens. Matter Phys., 13:275, 2022.
- [4] M. Xu, L. H. Kendrick, A. Kale, et al. Frustration- and doping-induced magnetism in a Fermi–Hubbard simulator. *Nature*, 620:971–976, 2023.
- [5] E. Ibarra-García-Padilla, R. Mukherjee, R. G. Hulet, K. R. A. Hazzard, T. Paiva, and R. T. Scalettar. Thermodynamics and magnetism in the twodimensional to three-dimensional crossover of the Hubbard model. *Phys. Rev.* A, 102(3):033340, 2020.
- [6] F. Sun and Y. X. Xiao. Boosting determinant quantum Monte Carlo with submatrix updates: Unveiling the phase diagram of the 3d Hubbard model. SciPost Phys., 18(2):055, 2025.
- [7] Q. Song, S. Stavrić, P. Barone, et al. Electrical switching of a *p*-wave magnet. *Nature*, 642:64–70, 2025.
- [8] R. Staudt, M. Dzierzawa, and A. Muramatsu. Phase diagram of the three-dimensional Hubbard model at half filling. *Eur. Phys. J. B*, 17:411–415, 2000.

- [9] F. Werner, O. Parcollet, A. Georges, and S. R. Hassan. Interaction-induced adiabatic cooling and antiferromagnetism of cold fermions in optical lattices. *Phys. Rev. Lett.*, 95(5):056401, 2005.
- [10] S. Fuchs, E. Gull, M. Troyer, M. Jarrell, and T. Pruschke. Spectral properties of the three-dimensional Hubbard model. *Phys. Rev. B*, 83(23):235113, 2011.
- [11] T. Schäfer, A. A. Katanin, K. Held, and A. Toschi. Interplay of correlations and Kohn anomalies in three dimensions: Quantum criticality with a twist. *Phys. Rev. Lett.*, 119(4):046402, 2017.
- [12] E. Kozik, E. Burovski, V. W. Scarola, and M. Troyer. Néel temperature and thermodynamics of the half-filled three-dimensional Hubbard model by diagrammatic determinant Monte Carlo. Phys. Rev. B, 87(20):205102, 2013.
- [13] R. Garioud, F. Šimkovic, R. Rossi, G. Spada, T. Schäfer, F. Werner, and M. Ferrero. Symmetry-broken perturbation theory to large orders in antiferromagnetic phases. *Phys. Rev. Lett.*, 132(24):246505, 2024.
- [14] I. Bloch. Ultracold quantum gases in optical lattices. Nat. Phys., 1:23, 2005.
- [15] D. P. Arovas, E. Berg, S. A. Kivelson, and S. Raghu. The hubbard model. Annu. Rev. Condens. Matter Phys., 13:239, 2022.
- [16] J. Hubbard. Electron correlations in narrow energy bands. Proc. R. Soc. London, Ser. A, 276:238, 1963.
- [17] M. C. Gutzwiller. Effect of correlation on the ferromagnetism of transition metals. Phys. Rev. Lett., 10:159, 1963.
- [18] J. Kanamori. Electron correlation and ferromagnetism of transition metals. *Prog. Theor. Phys.*, 30:275–289, 1963.
- [19] M. H. Anderson, J. R. Ensher, M. R. Matthews, C. E. Wieman, and E. A. Cornell. Observation of bose-einstein condensation in a dilute atomic vapor. *Science*, 269:198, 1995.

- [20] D. Jaksch, C. Bruder, J. I. Cirac, C. W. Gardiner, and P. Zoller. Cold bosonic atoms in optical lattices. *Phys. Rev. Lett.*, 81:3108, 1998.
- [21] B. DeMarco and D. S. Jin. Onset of fermi degeneracy in a trapped atomic gas. *Science*, 285:1703, 1999.
- [22] E. C. Stoner. Collective electron ferromagnetism. Proc. R. Soc. London, Ser. A, 165:372, 1938.
- [23] D. J. Thouless. Exchange in solid <sup>3</sup>he and the heisenberg hamiltonian. Proc. Phys. Soc., 86:893, 1965.
- [24] Y. Nagaoka. Ferromagnetism in a narrow, almost half-filled s band. Phys. Rev., 147:392, 1966.
- [25] H. Tasaki. Extension of nagaoka's theorem on the large-u hubbard model. *Phys. Rev. B*, 40:9192, 1989.
- [26] A. Mielke. Ferromagnetism in the hubbard model on line graphs and further considerations. J. Phys. A: Math. Gen., 24:3311, 1991.
- [27] E. Müller-Hartmann. Ferromagnetism in Hubbard models: Low density route. J. Low Temp. Phys., 99(3):349–354, 1995.
- [28] P. Pieri, S. Daul, D. Baeriswyl, et al. Low-density ferromagnetism in the Hubbard model. *Phys. Rev. B*, 54(13):9250–9253, 1996.
- [29] I. Bloch, J. Dalibard, and W. Zwerger. Many-body physics with ultracold gases. *Rev. Mod. Phys.*, 80:885, 2008.
- [30] L. Tarruell, D. Greif, T. Uehlinger, G. Jotzu, and T. Esslinger. Creating, moving and merging dirac points with a fermi gas in a tunable honeycomb lattice. *Nature*, 483:302, 2012.
- [31] J. Sebby-Strabley, M. Anderlini, P. S. Jessen, and J. V. Porto. Preparing and probing atomic number states with an atom interferometer. *Phys. Rev. Lett.*, 98:200405, 2007.

- [32] J. Yang, L. Liu, J. Mongkolkiattichai, and P. Schauss. Site-resolved imaging of ultracold fermions in a triangular-lattice quantum gas microscope. PRX Quantum, 2:020344, 2021.
- [33] J. Struck, C. Ölschläger, R. Le Targat, P. Soltan-Panahi, A. Eckardt, M. Lewenstein, P. Windpassinger, and K. Sengstock. Quantum simulation of frustrated classical magnetism in triangular optical lattices. *Science*, 333:996– 999, 2011.
- [34] G.-B. Jo, J. Guzman, C. K. Thomas, P. Hosur, A. Vishwanath, and D. M. Stamper-Kurn. Ultracold atoms in a tunable optical kagome lattice. *Phys. Rev. Lett.*, 108:045305, 2012.
- [35] R. Yamamoto, H. Ozawa, D. C. Nak, I. Nakamura, and T. Fukuhara. Single-site-resolved imaging of ultracold atoms in a triangular optical lattice. New J. Phys., 22:123028, 2020.
- [36] J. Trisnadi, M. Zhang, L. Weiss, and C. Chin. Design and construction of a quantum matter synthesizer. *Rev. Sci. Instrum.*, 93:083203, 2022.
- [37] C. Li, M. G. He, C. Y. Wang, et al. Frustration-induced itinerant ferromagnetism of fermions in optical lattices. *Phys. Rev. B*, 109, 2024.
- [38] L. Liu, H. Yao, E. Berg, S. R. White, and S. A. Kivelson. Phases of the infinite *U* Hubbard model on square lattices. *Phys. Rev. Lett.*, 108, 2012.
- [39] O. J. Amin, A. Dal Din, E. Golias, et al. Nanoscale imaging and control of altermagnetism in MnTe. *Nature*, 636:348–353, 2024.
- [40] E. Isufi Neziri, C. Hensky, H. Q. Le, D. Radillo Ochoa, A. Cebrat, M. Parschau, K.-H. Ernst, and C. Wäckerlin. 2d metalorganic ferromagnets. Adv. Sci., 12:2415266, 2025.
- [41] National Academies of Sciences, Engineering, and Medicine. The Current Status and Future Direction of High-Magnetic-Field Science and Technology in the United States. The National Academies Press, Washington, DC, 2024.

- [42] H. Zhou, M. dos Santos Dias, S. Bao, et al. Triple-q state in magnetic breathing kagome lattice. *npj Spintronics*, 3:31, 2025.
- [43] Francisco Lieberich et al. Probing and tuning geometric frustration in an organic quantum magnet via elastocaloric measurements under strain. *Sci. Adv.*, 11:eadz0699, 2025.
- [44] Wei Ren, Wei Li, Guofang Feng, Liting Jiang, Jing Gan, Yuyang Han, Xiaohua Luo, Changcai Chen, Chunsheng Fang, and Shengcan Ma. Large room temperature anomalous hall and nernst effects in kagomé ZrFe<sub>2</sub> ferromagnet. Materials Today Physics, 57:101838, 2025. arXiv:2507.07886v1 [cond-mat.str-el].
- [45] Revathy B S. Shaping magnetic order by local frustration for itinerant fermions on a graph. arXiv preprint, 2025. arXiv:2507.07886v1 [cond-mat.str-el].
- [46] A. May, M. Hunt, A. Van Den Berg, et al. Realisation of a frustrated 3d magnetic nanowire lattice. *Commun Phys*, 2:13, 2019.
- [47] V. M. Galitskii. The energy spectrum of a non-ideal Fermi gas. Sov. Phys. JETP, 7(1):104–112, 1958.
- [48] R. Hlubina, S. Sorella, and F. Guinea. Ferromagnetism in the two dimensional t–t′ Hubbard model at the van Hove density. *Phys. Rev. Lett.*, 78(7):1343–1346, 1997.
- [49] D. C. Mattis. The Theory of Magnetism Made Simple: An Introduction to Physical Concepts and to Some Useful Mathematical Methods. World Scientific Publishing Company, 2006.
- [50] R. R. Netz and A. N. Berker. Monte Carlo mean-field theory and frustrated systems in two and three dimensions. *Phys. Rev. Lett.*, 66(3):377–380, 1991.
- [51] R. R. Netz and A. N. Berker. Hard-spin mean-field theory: Formulation for Ising, XY, and other models. J. Appl. Phys., 70(10):6074–6076, 1991.

- [52] R. R. Netz and A. N. Berker. Smectic-c order, in-plane domains, and nematic reentrance in a microscopic model of liquid crystals. *Phys. Rev. Lett.*, 68(3):333–336, 1992.
- [53] E. H. Lieb and F. Y. Wu. Absence of Mott transition in an exact solution of the short-range, one-band model in one dimension. *Phys. Rev. Lett.*, 20(25):1445– 1449, 1968.
- [54] A. V. Gold, L. Hodges, P. T. Panousis, et al. de Haas-van Alphen studies of ferromagnetic iron and a model for its Fermi surface. *Int. J. Magn.*, 2:357–372, 1971.
- [55] M. B. Stearns. Why is iron magnetic? Phys. Today, 31(4):34–39, 1978.
- [56] M. B. Stearns. Simple explanation of tunneling spin-polarization of Fe, Co, Ni and its alloys. J. Magn. Magn. Mater., 5(2):167–171, 1977.
- [57] J. Kübler. Theory of Itinerant Electron Magnetism. Oxford University Press, 2021.
- [58] K. J. Duff and T. P. Das. Electron states in ferromagnetic iron. II. wavefunction properties. *Phys. Rev. B*, 3(7):2294–2306, 1971.
- [59] S. Allen, A. M. S. Tremblay, and Y. M. Vilk. Theoretical methods for strongly correlated electrons. 2003.
- [60] H. Fehske, R. Schneider, and A. Weisse, editors. *Computational Many-Particle Physics*, volume 739 of *Lecture Notes in Physics*. Springer, 2007.
- [61] V. Eijkhout. Introduction to High Performance Scientific Computing. Lulu.com, 2010.
- [62] J. Kiusalaas. Numerical Methods in Engineering with Python. Cambridge University Press, 2010.
- [63] S. Linge and H. P. Langtangen. Programming for Computations—A Gentle Introduction to Numerical Simulations with Python. 2016. Texto en línea: S. Linge and HP Langtangen: Programming for Computations.

- [64] J. M. Kinder and P. Nelson. A Student's Guide to Python for Physical Modeling. Princeton University Press, 2021.
- [65] C. Fuhrer, J. E. Solem, and O. Verdier. Scientific Computing with Python: High-performance scientific computing with NumPy, SciPy, and pandas. Packt Publishing Ltd, 2021.
- [66] T. H. Cormen, C. E. Leiserson, R. L. Rivest, et al. Introduction to Algorithms. MIT Press, 4th edition, 2022.
- [67] R. Hlubina. Phase diagram of the weak-coupling two-dimensional t-t' Hubbard model at low and intermediate electron density. *Phys. Rev. B*, 59(14):9600-9603, 1999.

## Acknowledgements

I want to thank Prof.Pierbiagio Pieri, for his continuous guidance, encouragement, and invaluable insights throughout the course of my research and the writing of this thesis. I also want to thank the professors in our department for their teaching and support during my studies. Their lectures and advice have greatly broadened my knowledge and provided me with the solid foundation necessary for this research. Finally, thanks to my family and friends, whose constant encouragement and understanding have accompanied me throughout this journey. Without their support, this work would not have been possible.